

A comparative analysis of SARS-CoV-2 antivirals in human airway models characterizes 3CL^{pro} inhibitor PF-00835231 as a potential new treatment for COVID-19

5 Maren de Vries¹, Adil S Mohamed¹, Rachel A Prescott^{1,2}, Ana M Valero-Jimenez¹,
6 Ludovic Desvignes^{3,4}, Rebecca O'Connor⁵, Claire Steppan⁵, Joseph C Devlin^{2,6}, Ellie
7 Ivanova⁷, Alberto Herrera⁷, Austin Schinlever^{1,2}, Paige Loose¹, Kelly Ruggles⁶, Sergei B
8 Koralov⁷, Annaliesa S. Anderson⁸, Joseph Binder⁹, and Meike Dittmann^{1#}

9 ¹ Department of Microbiology, New York University Grossman School of Medicine, New
10 York 10016, USA

11 ² Vilcek Institute of Graduate Biomedical Sciences, New York University Grossman
12 School of Medicine, New York 10016, USA

13 ³ Department of Medicine, New York University Grossman School of Medicine, New
14 York 10016, USA

15 ⁴Office of Science & Research, NYU Langone Health, New York 10016, USA

16 ⁵ Pfizer Discovery Sciences, Groton, CT 06340, USA

17 ⁶ Institute of Systems Genetics, New York University Grossman School of Medicine,
18 New York 10016, USA

19 ⁷ Department of Pathology, New York University Grossman School of Medicine, New
20 York 10016, USA

21 ⁸Pfizer Vaccine Research and Development, Pearl River, NY 10695, USA

22 ⁹Pfizer Oncology Research and Development, San Diego, CA 92128, USA

23 # corresponding author

24 Meike Dittmann, PhD

25 430 East 29th Street

26 NYU Grossman School of Medicine

27 Alexandria Center for Life Sciences – West Tower

28 430 East 29th Street, AW 3rd Floor, Room 313, New York, NY 10016

29 Phone: 646-501-4642

30 Meike.Dittmann@nyulangone.org

31

32 **Abstract**

33 Severe acute respiratory syndrome coronavirus 2 (SARS-CoV-2) is the etiological agent
34 of Coronavirus Disease 2019 (COVID-19). There is a dire need for novel effective
35 antivirals to treat COVID-19, as the only approved direct-acting antiviral to date is
36 remdesivir, targeting the viral polymerase complex. A potential alternate target in the viral
37 life cycle is the main SARS-CoV-2 protease 3CL^{pro} (M^{pro}). The drug candidate PF-
38 00835231 is the active compound of the first anti-3CL^{pro} regimen in clinical trials. Here,
39 we perform a comparative analysis of PF-00835231, the pre-clinical 3CL^{pro} inhibitor GC-
40 376, and the polymerase inhibitor remdesivir, in alveolar basal epithelial cells modified to
41 express ACE2 (A549^{+ACE2} cells). We find PF-00835231 with at least similar or higher
42 potency than remdesivir or GC-376. A time-of-drug-addition approach delineates the
43 timing of early SARS-CoV-2 life cycle steps in A549^{+ACE2} cells and validates PF-
44 00835231's early time of action. In a model of the human polarized airway epithelium,
45 both PF-00835231 and remdesivir potently inhibit SARS-CoV-2 at low micromolar
46 concentrations. Finally, we show that the efflux transporter P-glycoprotein, which was
47 previously suggested to diminish PF-00835231's efficacy based on experiments in
48 monkey kidney Vero E6 cells, does not negatively impact PF-00835231 efficacy in either
49 A549^{+ACE2} cells or human polarized airway epithelial cultures. Thus, our study provides *in*
50 *vitro* evidence for the potential of PF-00835231 as an effective SARS-CoV-2 antiviral and
51 addresses concerns that emerged based on prior studies in non-human *in vitro* models.

52 **Importance**

53 The arsenal of SARS-CoV-2 specific antiviral drugs is extremely limited. Only one direct-
54 acting antiviral drug is currently approved, the viral polymerase inhibitor remdesivir, and
55 it has limited efficacy. Thus, there is a substantial need to develop additional antiviral
56 compounds with minimal side effects and alternate viral targets. One such alternate target
57 is its main protease, 3CL^{pro} (M^{pro}), an essential component of the SARS-CoV-2 life cycle
58 processing the viral polyprotein into the components of the viral polymerase complex. In
59 this study, we characterize a novel antiviral drug, PF-00835231, which is the active
60 component of the first-in-class 3CL^{pro}-targeting regimen in clinical trials. Using 3D *in vitro*
61 models of the human airway epithelium, we demonstrate the antiviral potential of PF-
62 00835231 for inhibition of SARS-CoV-2.

63 **Introduction**

64 In December 2019, multiple cases of severe pneumonia with unexplained etiology were
65 reported in Wuhan, China¹. The infectious agent was identified as a novel member of the
66 family *Coronaviridae*¹, later named severe acute respiratory syndrome coronavirus 2
67 (SARS-CoV-2)². The resulting disease, Coronavirus Disease 2019 (COVID-19), has
68 since become a deadly pandemic.

69 A number of candidate drugs that may inhibit SARS-CoV-2 infection and replication have
70 been proposed. However, only one direct-acting antiviral is currently approved for the
71 treatment of COVID-19: remdesivir, a nucleoside analog that inhibits the SARS-CoV-2
72 RNA-dependent RNA-polymerase (RdRp). Remdesivir is incorporated into viral RNA by
73 the RdRp, resulting in chain termination of both viral transcripts and *de novo* synthesized
74 viral genomes³. Given this considerably limited arsenal of direct-acting antivirals for
75 COVID-19, it remains a strategic priority to develop novel compounds with minimal side
76 effects and that are directed against alternate viral targets.

77 One such alternate SARS-CoV-2 target is its main protease, 3CL^{pro} (M^{pro}), which plays
78 an essential role in the viral life cycle: Upon entry and uncoating of the viral particles, the
79 positive-stranded RNA genome is rapidly translated into two polyproteins which are
80 subsequently processed into functional proteins by PL2^{pro} and 3CL^{pro} viral proteases⁴.
81 3CL^{pro} is the main protease and is responsible for releasing 11 of the 13 individual
82 proteins, including the polymerase subunits, enabling their proper folding and assembly
83 into the active polymerase complex⁵. Thus, blocking 3CL^{pro} activity effectively shuts down
84 the life cycle before viral transcription or replication occur, making it an enticing target for
85 intervention⁶. In addition, 3CL^{pro} has a unique substrate preference (Leu-Gln ↓ {Ser, Ala,

86 Gly}), a preference not shared by any known human protease, implying the potential for
87 high selectivity and low side effects of 3CL^{pro}-targeting drugs⁷. Although there have been
88 intense efforts to develop 3CL^{pro} inhibitors specific for SARS-CoV-2⁶⁻¹³, only one inhibitor
89 has been brought to the clinic, PF-07304814, which is the first anti-3CL^{pro} compound in
90 clinical trials.

91 PF-07304814 is a ketone-based covalent cysteine protease inhibitor⁹. It is administered
92 as a phosphate prodrug, which is then metabolized to its active form, PF-00835231¹⁴. PF-
93 00835231 was initially designed in response to a previous coronavirus epidemic in 2003,
94 as an inhibitor for the 3CL^{pro} of SARS-CoV⁹. However, with SARS-CoV disease declining,
95 clinical studies were not practical and, consequently, PF-00835231 was never tested in
96 patients. Because 3CL^{pro} of SARS-CoV and SARS-CoV-2 are 96% identical at the amino
97 acid level, including 100% identity within the catalytic pocket⁷, it seemed reasonable to
98 assume that PF-00835231 may inhibit SARS-CoV-2 as well.

99 Indeed, a recent study demonstrated antiviral activity of PF-00835231 against SARS-
100 CoV-2, albeit at high micromolar levels¹⁴. The study was performed in Vero E6 cells, a
101 monkey kidney cell line in which SARS-CoV-2 replicates to high titers, but which is known
102 to express high levels of the efflux transporter P-glycoprotein (also known as Multi-Drug
103 Resistance Protein 1, MDR1, and encoded by gene ATP Binding Cassette Subfamily B
104 Member 1, *ABCB1*)¹⁵. Inhibiting MDR1 function significantly increased antiviral efficacy in
105 Vero E6 cells, suggesting that PF-00835231 is an MDR1 substrate¹⁴. MDR1 is well-
106 studied in the context of human immunodeficiency virus 1 (HIV-1) protease inhibitors such
107 as lopinavir or ritonavir, where it reduces intracellular protease inhibitor levels and
108 contributes to drug resistance in T-cells and monocytes¹⁶. In contrast to HIV-1, where

109 viral replication is essentially limited to T-cells and monocytes, SARS-CoV-2 infects
110 multiple organs and cell types throughout the human body, with the first and major site of
111 replication being cells of the respiratory tract^{17,18}. Thus, to investigate the potential role of
112 MDR1 on antiviral potency of PF-00835231 against SARS-CoV-2, it is imperative to utilize
113 experimental model systems representing the human airways.

114 Here, we characterize the antiviral potency and cytotoxicity profile of PF-00835231 in two
115 human airway models: a human type II alveolar epithelial cell line, and polarized human
116 airway epithelial cultures. In side-by-side experiments, we place PF-00835231's antiviral
117 efficacy against SARS-CoV-2 in context of another, pre-clinical 3CL^{pro} inhibitor, GC-376,
118 and of the current standard-of-care, remdesivir. Finally, we address the impact of P-
119 glycoprotein (MDR1) on PF-00835231's antiviral efficacy in the human airways.

120

121 **Results**

122 **Establishing A549^{+ACE2} cells as a tool to determine SARS-CoV-2 infection and**
123 **cytopathic effect by high-content microscopy.** The human adenocarcinoma alveolar
124 epithelial cell line A549 is a workhorse cell line in the study of respiratory viruses.
125 However, A549 cells are not permissive to SARS-CoV-2 infection, as they do not highly
126 express the SARS-CoV-2 receptor ACE2¹⁹. To make A549 cells amenable for
127 experiments with SARS-CoV-2, we generated a stable A549 cell line expressing ACE2
128 exogenously. We confirmed elevated levels of ACE2 mRNA in A549^{+ACE2} cells by RT-
129 qPCR, and of ACE2 protein by Western blot, flow cytometry, and confocal microscopy
130 (Fig. 1a-e).

131 To determine permissiveness, we infected A549 or A549^{+ACE2} cells with a serial dilution
132 of SARS-CoV-2, in a 96-well format, for 24 h. Using immunofluorescence staining for
133 SARS-CoV-2 nucleocapsid protein (N) and high-content microscopy, we found A549^{+ACE2}
134 cells permissive to SARS-CoV-2 infection, whereas parent A549 cells were not (Fig. 1f).

135 Since the discovery of SARS-CoV-2, limited evolution has been observed, which has
136 been attributed to the proof-reading mechanism of coronavirus polymerases²⁰. The two
137 major lineages of SARS-CoV-2 circulating globally as of time of writing are represented
138 by the Wuhan basal clade and the spike protein D614G clade, also referred to as clades
139 A and B, respectively²¹. Compared to clade A, clade B isolates carry a mutation in the
140 spike-encoding gene S, which results in amino acid substitution D614G. D614G is
141 frequently accompanied by an additional mutation in ORF 1b, which encodes the RNA-
142 dependent RNA-polymerase complex (RdRp), resulting in substitution P323L in the
143 polymerase subunit NSP12²². Clade B viruses are more prevalent globally, which might

144 be due to their increased efficiency infecting cells in the upper respiratory tract and
145 subsequently increased transmissibility, enabled by the Spike D614G mutation^{23,24}.
146 To characterize viral growth of representatives from the two major clades in our model,
147 we challenged A549^{+ACE2} cells with the clinical SARS-CoV-2 isolate USA-WA1/2020, a
148 clade A representative²⁵, or with USA/NYU-VC-003/2020, a clade B representative, the
149 latter of which we had isolated in March 2020²⁶. USA/NYU-VC-003/2020 carries both of
150 the signature clade B amino acid changes, S D614G and NSP12 P323L, but its 3CL^{pro}
151 sequence is identical to that of USA-WA1/2020. In low MOI growth kinetics on A549^{+ACE2}
152 cells, we found that growth of clade B USA/NYU-VC-003/2020 exceeds that of clade A
153 USA-WA1/2020, especially at later times of infection (Fig. 1g). We were able to detect *de*
154 *novo* produced infectious particles as soon as 12 hours post infection (hpi) for USA-
155 WA1/2020, suggesting that the SARS-CoV-2 life cycle in A549^{+ACE2} cells is completed by
156 that time. In terms of producing infectious titers, USA/NYU-VC-003/2020 initially lagged
157 behind USA-WA1/2020, but then yielded significantly higher titers at 48 and 72 hpi.
158 Finally, we observed that the cytopathic effect (CPE) caused by SARS-CoV-2 on
159 A549^{+ACE2} cells manifests in syncytia formation, in which the nuclei form a ring-like
160 structure (Fig. 1h). This effect had previously been described for other coronaviruses^{27,28},
161 although the exact mechanism for the ring-like nuclear structure formation remains to be
162 elucidated. Altogether, our data establish A549^{+ACE2} cells as a tractable tool to study
163 SARS-CoV-2 infection, spread, and cytopathic effect.

164
165 **PF-00835231 potently inhibits SARS-CoV-2 in A549^{+ACE2} cells.** PF-00835231 is the
166 active compound of the first anti 3CL^{pro} regimen currently tested in clinical trials⁹. We
167 studied and compared three compounds in regards to SARS-CoV-2 antiviral activity and

168 cytotoxicity: i. PF-00835231, ii. the pre-clinical 3CL^{pro} inhibitor GC-376, which is licensed
169 for veterinary use in Feline Coronavirus infections²⁹ and recently shown to inhibit SARS-
170 CoV-2 in Vero E6 cells²⁶, and iii. the polymerase inhibitor remdesivir, which is currently
171 the only direct-acting antiviral approved in the US to treat SARS-CoV-2 infections, and is
172 thus standard-of-care. We exposed A549^{+ACE2} cells with escalating doses of the three
173 respective drugs, challenged them with SARS-CoV-2, and measured virus antigen (N)-
174 expressing cells by high-content microscopy (Fig. 2a). In parallel, we determined cellular
175 viability by measuring ATP levels in drug-treated, but uninfected cells. Antiviral assays
176 were performed with both our clade A and clade B SARS-CoV-2 representatives.
177 In a first set of experiments, we compared antiviral efficacy between PF-00835231 and
178 remdesivir side-by-side (Fig. 2 and Tab.1). PF-00835231 inhibited the clade A
179 representative SARS-CoV-2 USA-WA1/2020 with an average 50% effective
180 concentration (EC₅₀) of 0.221 µM at 24 h, and 0.158 µM at 48 h (Fig. 2b, Tab. 1). As such,
181 PF-00835231 was statistically more potent than remdesivir with an EC₅₀ 0.442 µM at 24
182 h, and 0.238 µM at 48 h (Fig. 2c, Tab. 1). None of the compounds showed detectable
183 cytotoxicity (Fig. 2b-e, Tab. 1). We then compared antiviral efficacy of PF-00835231 and
184 remdesivir for clade B USA/NYU-VC-003/2020. Due to cytopathic effects driven by
185 USA/NYU-VC-003/2020 at the 48 h timepoint, we only determined antiviral efficacy at 24
186 h. PF-00835231 was inhibitory with an EC₅₀ of 0.184 µM, and was thus again statistically
187 more potent than remdesivir with EC₅₀ of 0.283 µM.
188 Interestingly, only the polymerase inhibitor remdesivir exhibited statistically significantly
189 weaker antiviral activity against the clade A isolate compared to the clade B isolate, with
190 EC₅₀ of 0.442 µM (vs clade A) and EC₅₀ of 0.238 µM (vs clade B; Tab. 1). This might be

191 an impact of the polymerase subunit NSP12 P323L mutation present in the clade B
192 representative. Next, we analyzed microscopy data for drug-mediated inhibition of the
193 CPE, including ring-shaped syncytia formation. PF-00835231 and remdesivir both
194 decreased the overall number of infected foci, and fully protected A549^{+ACE2} cells from
195 ring syncytia formation, at 0.33 μ M and above (Fig. 2f and not shown).

196 In a second set of experiments, we compared antiviral efficacy between PF-00835231
197 and GC-376 side-by-side (Fig. 3a-d and Tab. 2). PF-00835231 inhibited the clade A
198 representative SARS-CoV-2 USA-WA1/2020 with an EC₅₀ of 0.422 μ M at 24 h, and 0.344
199 μ M at 48 h (Fig. 2a, Tab. 1). This slight shift in EC₅₀ values as compared to those in Table
200 1 can be explained by intra-assay variation, which is higher for live cell assays as it is for
201 binding assays. For this reason we could not compare PF-00835231 across assays. In
202 the direct comparison, PF-00835231 trended towards being more potent than GC-376,
203 which exhibited an EC₅₀ of 0.632 μ M at 24 h, and 0.696 μ M at 48 h (Fig. 3b, Tab. 2). For
204 clade B USA/NYU-VC-003/2020, PF-00835231 was inhibitory with an EC₅₀ of 0.326 μ M,
205 and thus again trended towards being more potent than GC-376 with an EC₅₀ of 0.529
206 μ M (Fig. 3c-d, Tab. 2).

207 Both protease inhibitors PF-00835231 and GC-376 had similar antiviral activities between
208 the two clades in this assay (Tab. 1 and Tab. 2). This is in line with the fact that 3CL^{pro} is
209 identical in these two viruses. Finally, GC-376 decreased the number and size of viral
210 foci, but was unable to protect cells from virus-induced CPE at 1 μ M (Fig. 3e). In contrast,
211 at 1 μ M and above, PF-00835231 fully protected A549^{+ACE2} cells from CPE (Fig. 3e and
212 not shown).

213 Collectively, we show that, in this assay, PF-00835231 inhibits isolates from both major
214 SARS-CoV-2 lineages at similar or better effective concentrations than remdesivir and
215 the pre-clinical 3CL^{pro} inhibitor GC-376.

216

217 **Timing of PF-00835231 antiviral action against USA-WA1/2020 in A549^{+ACE2} cells is**
218 **consistent with PF-00835231's role as a 3CL^{pro} inhibitor.** PF-00835231 and
219 remdesivir target different SARS-CoV-2 proteins^{9,31}. PF-00835231 targets 3CL^{pro},
220 blocking polyprotein processing and thus formation of the viral polymerase complex³².
221 Remdesivir acts on the subsequent step, which is the incorporation of nucleotides into
222 nascent viral RNA transcripts and genomes by the viral polymerase complex^{3,33}.

223 To determine whether the action of PF-00835231 is consistent with its established role
224 as a 3CL^{pro} inhibitor, and to delineate the timing of early SARS-CoV-2 life cycle stages in
225 A549^{+ACE2} cells, we performed time-of-drug-addition experiments³⁴. This approach
226 determines how long the addition of a drug can be delayed before it loses antiviral activity.
227 Using one-hour-increments (from 1 h prior to 4 h post infection), we varied the time-of-
228 drug-addition for a monoclonal neutralizing antibody (viral attachment inhibition control),
229 GC-376 (3CL^{pro} inhibition control), PF-00835231, and remdesivir (RdRp inhibition
230 control). We measured the percentage of SARS-CoV-2-infected cells via high-content
231 microscopy at 12 hpi, which corresponds to one replication cycle in A549^{+ACE2} cells, as
232 determined previously (Fig. 1g). We synchronized infection using a preincubation step at
233 4°C, followed by a transition to 37° C at 1 h post-addition of virus, and used the minimum
234 treatment doses for each drug that led to undetectable infection levels – 3 µM for PF-
235 00835231 and the neutralizing antibody, and 10 µM for remdesivir and GC-376.

236 The neutralizing antibody lost its antiviral function first, starting at the first addition point
237 post-infection (1 h), confirming blockage of attachment and entry as the mode of antiviral
238 action (Fig. 4a). Interestingly, all three drugs, GC-376, PF-00835231, and remdesivir lost
239 antiviral action at the same time of addition, starting at 2 hpi, and with subsequently
240 enhanced loss of activity at 3 and 4 hpi (Fig. 4a). This suggests that polyprotein
241 processing and the start of viral transcription / translation follow each other very closely
242 in time. These time-of-drug-addition experiments confirm the timing of PF-00835231's
243 antiviral action during the early stages of intracellular virus propagation, consistent with
244 its role as a 3CL^{pro} inhibitor. Furthermore, these experiments delineate the timing of the
245 SARS-CoV-2 life cycle events in the tissue culture model of A549^{+ACE2} cells (Fig. 4b) and
246 demonstrate that polymerase and protease inhibitors such as PF-00835231 can
247 effectively block SARS-CoV-2 replication in cells when administered within a few hours
248 after infection.

249

250 **PF-00835231 is well-tolerated in polarized human airway epithelial cultures (HAEC).**
251 The human respiratory tract is a major entry portal for viruses, including SARS-CoV-2,
252 and the first battle between host and virus occurs in cells of the respiratory epithelium.
253 This specialized tissue contains three major cell types (basal, secretory, and ciliated)
254 which are organized in a characteristic polarized architecture³⁵. As shown, human
255 adenocarcinoma alveolar epithelial A549^{+ACE2} cells are permissive for SARS-CoV-2
256 infection and allow for high-throughput experiments (Fig. 1-4). However, they do not
257 recapitulate the complexity and architecture of the human airway epithelium.

258 To test PF-00835231 and remdesivir in an additional, more physiologically relevant, yet
259 lower-throughput human model system, we generated polarized human airway epithelial
260 cultures (HAEC). HAEC contain multiple cell types of the airway epithelium and
261 recapitulate its typical architecture (Fig. 5a-d), which makes HAEC arguably one of the
262 most physiologically relevant models for *in vitro* studies of human respiratory pathogens.
263 HAEC are permissive to SARS-CoV-2 infections and were utilized to obtain the very first
264 SARS-CoV-2 isolate in December 2019¹.

265 First, we performed in-depth analyses of the cellular heterogeneity of our HAEC model
266 system by single-cell RNA-sequencing (sc-RNAseq; Fig. 5b³⁸). Gene-expression profiling
267 enabled resolution of distinct clusters with cell types assigned based on previously
268 published transcriptional signatures^{36,37}. We identified 7 different clusters as cycling
269 basal, basal, suprabasal, secretory, ciliated, and microfold cells, as well as cells
270 undergoing epithelial-mesenchymal transition (EMT, Fig. 5b). The EMT process in HAEC
271 has previously been associated with loss of polarized organization as a consequence of
272 remodeling³⁹ and is likely to occur at a low level at steady-state in HAEC. Recapitulation
273 of the major cell types and physiological conditions of the lung epithelium provided
274 molecular confirmation for the HAEC system in assessing SARS-CoV-2 infection.

275 To establish the use of PF-00835231 in HAEC, we determined its cytotoxicity profile and
276 compared it to that of remdesivir. We added PF-00835231 or remdesivir to the basolateral
277 chamber of HAEC (Fig. 5a), and determined tissue morphology by histology and integrity
278 of the epithelial layer by measuring trans-epithelial resistance (TEER; Fig. 5c-e). Neither
279 drug caused measurable adverse effects on the morphology of the cultures (Fig. 5c,d).
280 However, while remdesivir negatively impacted TEER over time, albeit not statistically

281 significantly compared to untreated cultures, we did not observe this trend for PF-
282 00835231 (Fig. 5e).

283 To complement our assessment of how well human epithelium tolerates these inhibitors,
284 we took advantage of an alternative cytotoxicity assay on BCi-NS1.1 cells, the basal-like
285 undifferentiated precursor cell monolayers used for generation of HAEC. We treated
286 these monolayers with a dose range of PF-00835231 or remdesivir for 48 hours, and
287 quantified ATP as a measure of cell viability, similar to previous experiments with
288 A549^{+ACE2} cells. We did not detect a decrease in ATP upon PF-00835231 treatment, even
289 at the highest amount of drug (10 μ M) tested. In contrast, 10 μ M of remdesivir caused a
290 reduction in ATP levels compared to carrier control, albeit not statistically significantly
291 (Fig. 5f). These experiments demonstrate that both drugs are well-tolerated in our model
292 of polarized human airway epithelium.

293

294 **PF-00835231 exhibits potent anti-SARS-CoV-2 activity in HAEC.** To determine PF-
295 00835231's anti-SARS-CoV-2 activity in HAEC, we added either 0.025, 0.5 or 10 μ M PF-
296 00835231 or remdesivir, or DMSO carrier control, to the basolateral chamber of HAEC
297 (Fig. 6a-c). We then challenged HAEC apically with SARS-CoV-2 USA-WA1/2020, and
298 determined viral infectious titers from apical washes collected at 12-hour increments.

299 We first detected progeny viral particles in apical washes from DMSO-treated cultures at
300 12 hpi (Fig. 6a, b), indicating that the SARS-CoV-2 life cycle in HAEC cells is completed
301 by that time. Both PF-00835231 and remdesivir potently inhibited SARS-CoV-2 titers in a
302 dose-dependent manner, with the 10 μ M doses resulting in viral titers below the limit of
303 detection at most time points (Fig. 6a, b).

304 To visualize SARS-CoV-2 infection in HAEC during drug treatment, we fixed infected
305 HAEC at the 72 h endpoint and stained them for SARS-CoV-2-N-expressing cells (Fig.
306 6c). In carrier control cultures, we observed robust infection. Upon treatment with 10 μ M
307 PF-00835231 or remdesivir, we found in both cases the number of infected cells
308 significantly reduced. Taken together, both remdesivir and PF-00835231 potently inhibit
309 SARS-CoV-2 infection in our model of polarized human airway epithelium.

310

311 **Inhibiting the multi-drug transporter MDR1 does not increase efficacy of PF-
312 00835231 in human airway epithelial cells.** Previously, a hurdle in accurately
313 determining PF-00835231's *in vitro* efficacy was the action of the multi-drug efflux
314 transporter P-glycoprotein (also known as MDR1 or *ABCB1*). However, these earlier
315 studies were performed in the monkey kidney cell line Vero E6^{9,14}. MDR1 was found to
316 efficiently export PF-00835231, thereby reducing intracellular PF-00835231 levels, and
317 likely underestimating PF-00835231's potency. In those studies, chemical inhibition of
318 MDR1 in Vero E6 cells significantly increased PF-00835231's antiviral efficacy^{9,14}.

319 Given the previously reported species differences in P-glycoprotein-mediated drug
320 transport activity of MDR1 and the variability in expression levels of the *ABCB1* gene that
321 encodes this drug transporter among cell types and tissues⁴⁰, we sought to determine a
322 potential role of MDR1 in our human *in vitro* airway models. We measured PF-00835231
323 anti-SARS-CoV-2 activity while chemically blocking MDR1 function, using the drug CP-
324 100356 in the A549^{+ACE2} cell line and in HAEC (Fig. 7a). We observed no changes in
325 antiviral efficacy when blocking MDR1 activity (Fig. 7b-d), suggesting that, in contrast to
326 Vero E6 cells, this transporter does not play a role in our human airway model systems.

327 Indeed, scRNA-seq analysis of HAECs (Fig. 5b³⁸) did not reveal any detectable MDR1
328 (ABCB1) transcripts, suggesting levels of this transporter in HAEC are low.

329 A limitation of the previous experiments is that A549 cells originate from one patient, and
330 HAEC were differentiated from precursor cells obtained from a single donor⁴¹. As a result,
331 we cannot exclude that human genetic variation might influence MDR1 function or
332 expression. Single nucleotide polymorphisms (SNPs) in the ABCB1 promoter or within
333 the open reading frame are well-described in the literature¹⁵. Furthermore, an inherent
334 limitation of sc-RNAseq is that only abundant transcripts are detected, and given limited
335 cellular heterogeneity of HAEC, it is possible that ABCB1 transcripts remained undetected
336 due to the limited depth of sequencing at single cell level.

337 To address these issues, we investigated transcript levels of ABCB1 in bronchoalveolar
338 lavages (BAL) of healthy individuals and of COVID-19 patients with mild or severe
339 symptoms from a previously published dataset^{42,43}. BAL contained multiple cell types,
340 including airway epithelial cells, but also immune cells, such as macrophages, T-cells,
341 plasma cells, and neutrophils (Fig. 7e). In healthy individuals, we detected MDR1
342 (ABCB1) in 1.77 % of CD8+/NK cells, 0.59% of proliferating T-cells, and 0.06% of
343 alveolar macrophages, but not in other cell types. Notably, we did not observe any ABCB1
344 transcript in airway epithelial cells, which are thought to be the major site of SARS-CoV-
345 2 replication^{17,18,44,45}. Compared to BAL from healthy individuals, BAL from COVID-19
346 patients with mild or severe symptoms showed an increased number of cells with
347 detectable levels of MDR1 (ABCB1) transcripts (Fig. 7f). Interestingly, rather than an
348 overall increase in ABCB1 gene expression, this upregulation was limited to a small
349 subset of individual cells, with the majority of cells remaining ABCB1-negative. This

350 phenomenon was observed in alveolar macrophages (0.25%/0.28% positive in
351 mild/severe COVID-19 patients), SPP1+ macrophages (0.23%/0.23%), M1-like
352 macrophages (2.60%/0.43%), CD8+/NK cells (7.75%/4.18%), proliferating T-cells
353 (2.00%/3.60%), plasma cells (cells not detected/0.74%), neutrophils (0%/0.05%) and in
354 epithelial cells (0.29%/0.18%). Our findings suggest that although MDR1 (*ABCB1*) is
355 upregulated in some cells during inflammatory processes such as observed in COVID-
356 19, its expression remains cell type-specific, and only a small fraction of airway epithelial
357 cells, the main replication sites for SARS-CoV-2, exhibit detectable levels of this efflux
358 transporter.

359 Thus, we conclude that MDR1 is unlikely to significantly impact PF-00835231 efficacy
360 during SARS-CoV-2 infection of the respiratory epithelium. In addition, our findings
361 highlight the importance of using appropriate *in vitro* models for the evaluation of antiviral
362 drugs.

363 **Discussion**

364 The current public health emergency caused by COVID-19 has illustrated our dire need
365 for vaccines and therapeutics to combat SARS-CoV-2. The SARS-CoV-2 polymerase
366 complex is the target of the majority of small molecule inhibitors in multiple stages of
367 development, including remdesivir³¹, favipiravir²⁰, and β -d-N4-hydroxycytidine⁴⁶. At the
368 time of writing, remdesivir is the only antiviral drug authorized for the treatment of COVID-
369 19. In contrast to the abovementioned compounds, PF-00835231 blocks the SARS-CoV-
370 2 3CL^{pro} protease⁹. PF-00835231 is the active component of PF-07304814, a first-in-class
371 SARS-CoV-2 3CL^{pro} inhibitor currently in clinical trials. Here, we report the potent antiviral
372 activity of PF-00835231 against SARS-CoV-2 in human lung epithelial cells and a model
373 of polarized human airway epithelial cultures (HAEC). In our A549^{+ACE2} cell assay, we
374 show that PF-00835231 has at least similar or better potency than the pre-clinical 3CL^{pro}
375 inhibitor GC-376, or remdesivir. In HAEC, we find both remdesivir and PF-00835231
376 similarly potent.

377 The lack of inhibitors specific to SARS-CoV-2 early in the pandemic prompted off-label
378 testing of protease inhibitors approved for other viruses, albeit with limited success⁴⁷. This
379 failure highlighted the need for novel compounds of greater specificity. A number of 3CL^{pro}
380 inhibitors have since been identified and characterized in *in vitro* assays, including the
381 cancer drug carmofur (1-hexylcarbamoyl-5-fluorouracil)¹², an alpha-ketoamide inhibitor
382 named 13b⁷, and a dipeptide-based inhibitor named GC-376⁴⁸. GC-376, licensed for
383 veterinary use²⁹, was recently shown to inhibit SARS-CoV-2 in Vero E6 cells at an EC₅₀
384 of 0.9 μ M¹¹. A different study showed PF-00835231 to inhibit SARS-CoV-2 at an EC₅₀ of
385 0.27 μ M in Vero E6 cells⁹. As such a comparison of historical data is problematic, we

386 directly compared the antiviral efficacy of PF-00835231 and GC-376 side-by-side in the
387 same assay (Fig. 3). We find that PF-00835231 is more potent than GC-376 in inhibiting
388 SARS-CoV-2 and protecting cells from CPE. This result illustrates the *in vitro* potency of
389 PF-00835231 compared to other, preclinical, 3CL^{pro} inhibitors, such as GC-376.

390 In coronaviruses, the genetic barrier to standard-of-care remdesivir or the pre-clinical drug
391 β -d-N4-hydroxycytidine is high, as mutations conferring resistance significantly reduce
392 viral fitness, and cross-resistance between remdesivir or β -d-N4-hydroxycytidine has not
393 been documented^{33,46}. A high resistance barrier to 3CL^{pro}-targeting drugs due to a high
394 fitness cost has also been demonstrated for the beta-coronavirus murine hepatitis virus
395 (MHV)⁴⁹. Although the likelihood of selecting for resistant variants seems thus low, the
396 existence of drugs with alternate targets may have important advantages. First, as seen
397 in other acute and chronic viral infections, blocking multiple targets in combination therapy
398 further decreases the likelihood for selection of viral resistance mutants^{50–52}. Second,
399 combination therapy with a cocktail of multiple drugs tackling different steps of the viral
400 life cycle may have synergistic effects on controlling viral replication. Indeed, a recent *in*
401 *vitro* study demonstrated significant synergistic effects between PF-00835231 and
402 remdesivir in inhibiting SARS-CoV-2¹⁴. Third, upon failure of monotherapy, it is preferable
403 to switch to an antiviral with a different target to circumvent cross-resistance caused by
404 mutations in the same target^{50–52}. For these reasons, the development of a diverse
405 toolbox of antiviral drugs with different targets will be important to improve antiviral
406 therapy in COVID-19.

407 The optimal window of opportunity for starting a successful antiviral drug regimen during
408 acute viral infections, such as influenza, is the first few days post-symptom onset, while

409 viral replication is actively ongoing⁵³. For most COVID-19 patients, this window is likely
410 limited to the first week of symptoms⁵⁴. Such early treatment with remdesivir is impeded
411 by its need for intravenous (IV) administration, requiring a healthcare facility setting,
412 though it still demonstrated benefit for 68% of patients with more advanced infection in
413 randomized clinical studies⁵⁵. PF-07304814, with its active component PF-00835231
414 evaluated in this study, is also an IV treatment⁹. However, the time of active SARS-CoV-
415 2 replication might be prolonged in the most severe patients, as suggested by the
416 aforementioned clinical data of remdesivir⁵⁵. This suggests the usefulness of SARS-CoV-
417 2 antiviral regimens even at later times of infection, which further supports the
418 investigation of PF-00835231 for the treatment of COVID-19.

419 P-glycoprotein (also known as MDR1, and encoded by gene *ABCB1*)⁹, is a membrane-
420 associated ATP-dependent efflux pump capable of removing cytostatic drugs from target
421 cells. The endogenous function of this transporter remains to be fully elucidated, but it is
422 expressed across several immune cell types and other metabolically active cells. P-
423 glycoprotein appears to be critical for maintenance and effector function of a range of
424 cytotoxic immune cells⁵⁶⁻⁵⁹. Two recent studies suggested that PF-00835231 is a
425 substrate for P-glycoprotein. This might pose a concern regarding the bioavailability of
426 PF-00835231 in SARS-CoV-2-infected cells. We addressed this concern in two ways:
427 functionally, by using chemical inhibition of MDR1 in human airway models, and
428 transcriptionally, by determining the expression of *ABCB1* in HAEC or in cells obtained
429 from BAL of healthy or COVID-19 patients. Our combined results demonstrate that MDR1
430 function does not impact PF-00835231 efficacy in our model systems, and is expressed
431 at very low levels in airway epithelial cells, which are the major sites of SARS-CoV-2

432 replication^{17,18,44,45}. By mining scRNA-seq data from BAL of COVID-19 patients and
433 healthy controls (n=12) for *ABCB1* expression, we considered the genetic variability on
434 the *ABCB1* locus beyond that present in our two model systems. Indeed, a number of
435 SNPs have been shown to alter expression of *ABCB1* transcripts, either by changing
436 transcription factor or micro-RNA binding sites upstream of the *ABCB1* open reading
437 frame, or by enhancing mRNA transcription due to silent mutations within the *ABCB1*
438 open reading frame¹⁵. Other, missense, mutations within the *ABCB1* open reading frame
439 have been shown to alter the functionality of MDR1, i.e. by altering membrane localization
440 or recycling of the protein, or by modifying substrate recognition sites^{15,60}. Although we
441 do not have information on the *ABCB1* genotype of our mined patient samples, the
442 detected low expression of *ABCB1* transcripts in the cells permissive for SARS-CoV-2,
443 together with the functional data from our model system, instills confidence that PF-
444 00835231 efficacy is not hampered by the action of MDR1.

445 Spillovers of zoonotic coronaviruses with high pathogenic potential into the human
446 population are not isolated events, as repeatedly illustrated by the emergence of SARS-
447 CoV in 2002, Middle East Respiratory Syndrome Coronavirus (MERS-CoV) in 2012, and
448 now SARS-CoV-2 in 2019⁶¹. To prepare for future pandemics, the development of pan-
449 coronavirus compounds is of strategic importance. This involves choosing viral targets
450 that are highly conserved within the coronavirus family, such as the 3CL^{pro} protease⁷.
451 Indeed, a recent study performing in vitro protease activity assays with PF-00835231
452 revealed potent inhibition across a panel of diverse coronavirus 3CL^{pro}, including those of
453 alpha-coronaviruses (NL63-CoV, PEDV, FIPV), beta-coronaviruses (HKU4-CoV, HKU5-
454 CoV, HKU9-CoV, MHV-CoV, OC43-CoV, HKU1-CoV), and a gamma-coronavirus (IBV-

455 CoV)¹⁴. Our study revealed that the two 3CL^{pro} inhibitors tested (PF-00835231 and GC-
456 376) were similarly potent for different clades of SARS-CoV-2 in which 3CL^{pro} is 100 %
457 conserved. Of note, 3CL^{pro} is also 100 % conserved in the SARS-CoV-2 “UK variant”
458 B.1.1.7 and the “Brazil variant” B.1.1.28, whereas the “South African variant” B.1.352
459 carries amino acid substitution K90R^{62–64}. However, the K90 residue is distant from the
460 active center of the protease, and is not expected to influence 3CL^{pro} substrate specificity.
461 These findings support the notion that PF-00835231 is an inhibitor with broad coronavirus
462 activity, which may be of use for emerging SARS-CoV-2 variants and for other emerging
463 coronaviruses beyond SARS-CoV-2.

464 Together, our data from two human in vitro model systems for SARS-CoV-2 show efficient
465 PF-00835231 antiviral activity and mitigate concerns arising from non-human models
466 such as Vero E6 cells regarding PF-00835231 counteraction by the efflux transporter P-
467 glycoprotein. Our results therefore inform and reinforce the ongoing clinical studies of pro-
468 drug PF-07304814 and its active form PF-00835231 as a potential new treatment for
469 COVID-19.

470 **Methods**

471 **Study design.** The primary goal of this study was to compare the *in vitro* efficacy and
472 cytotoxicity of PF-00835231 and remdesivir in two human model systems for SARS-CoV-
473 2 infection, A549^{+ACE2} cells and polarized human airway epithelial cultures. Compound
474 characterization at NYU was done in a blinded manner. If not stated otherwise, all assays
475 were performed in n=3 biological replicates. First, we performed in-depth characterization
476 of A549^{+ACE2} cells for the study of SARS-CoV-2, using RT-qPCR, western blotting, flow
477 cytometry, microscopy, and high-content imaging. Second, we evaluated the *in vitro*
478 efficacy and cytotoxicity of PF-00835231, of a second, pre-clinical, protease inhibitor, GC-
479 376, and of remdesivir in A549^{+ACE2} cells. We performed antiviral assays with SARS-CoV-
480 2 from the two major clades during the first year of the COVID-19 pandemic. Third, we
481 performed time-of-drug-addition assays in A549^{+ACE2} cells to delineate the time of antiviral
482 action for PF-00835231, remdesivir and GC-376 within the SARS-CoV-2 life cycle.
483 Fourth, we assessed the *in vitro* efficacy and cytotoxicity of PF-00835231 and remdesivir
484 in the physiologically relevant model of polarized human airway epithelial cultures. Finally,
485 we determined the role of efflux transporter MDR1 on the antiviral efficacy of PF-
486 00835231. Our studies were intended to generate the data required to assess further pre-
487 clinical investigations and the launch of a phase 1b clinical trial with PF-00835231 as a
488 base-compound for the potential treatment of COVID-19.

489

490 **Cells and viruses.** A549 cells were purchased from ATCC (cat no. CCL-185). To
491 generate A549^{+ACE2} cells, we cloned the human ACE2 cDNA sequence
492 (NP_001358344.1) into a pLV-EF1a-IRES-Puro backbone vector (Addgene, cat no.

493 85132), and prepared lentiviral particles as described previously⁶⁵. A549 cells were
494 transduced with pLV-EF1 α -hACE2-IRES-Puro lentivirus and bulk-selected for transduced
495 cells using 2.5 μ g/mL puromycin. A549^{+ACE2} cells were maintained in DMEM (Gibco, cat
496 no. 11965-092) containing 10% FBS (Atlanta Biologicals, cat no. S11150) (complete
497 media), and puromycin (2.5 μ g/mL final) was added to the media at every other passage.
498 A549^{+ACE2} cells were used for SARS-CoV-2 infection studies. Vero E6 cells, purchased
499 from ATCC (cat no. CLR-1586), were maintained in DMEM (Gibco, cat no. 11965-092)
500 containing 10% FBS (Atlanta Biologicals, cat no. S11150), and were used for growing
501 SARS-CoV-2 stocks and for SARS-CoV-2 plaque assays. Basal-like human airway
502 progenitor cells (Bci-NS1.1⁴¹) were obtained from Dr. Ronald G. Crystal and were used
503 for cytotoxicity assays and for the generation of polarized human airway epithelial cultures
504 (HAEC). They were maintained in BEGM Medium (Lonza, cat no. CC-3171 and CC-4175)
505 for cytotoxicity assays, while Pneumacult Ex Plus medium (StemCell, cat no. 05040) was
506 used to culture Bci-NS1.1 cells for the generation of human airway epithelial cultures.
507 All SARS-CoV-2 stock preparations and following infection assays were performed in the
508 CDC/USDA-approved BSL-3 facility in compliance with NYU Grossman School of
509 Medicine guidelines for biosafety level 3. SARS-CoV-2 isolate USA-WA1/2020, deposited
510 by the Center for Disease Control and Prevention, was obtained through BEI Resources,
511 NIAID, NIH (cat no. NR-52281, GenBank accession no. MT233526). The USA-WA1/2020
512 stock, obtained at passage 4, was passaged once in Vero E6 cells to generate a passage
513 5 working stock (1.7E + 06 PFU/mL) for our studies on A549^{+ACE2}. For studies on human
514 airway epithelial cultures, passage 5 USA-WA1/2020 was amplified once more in Vero
515 E6 cells and concentrated using an Amicon Ultra-15 centrifugal filter unit with a cut off of

516 100 kDa, resulting in a passage 6 working stock of 1.08E + 07 PFU/mL. SARS-CoV-2
517 USA/NYU-VC-003/2020 was isolated from patient nasal swab material in March 2020
518 (GenBank accession no. MT703677). We inoculated Vero E6 cells with a 1:2 dilution
519 series of the nasal swab material in infection media (DMEM 2% FBS, 1% Pen/Strep, 1%
520 NEAA, 10mM HEPES) to obtain passage 0 (P0) stock. P0 was passaged twice in Vero
521 E6 to generate a passage 2 working stock (1.1E + 07 PFU/mL) for drug efficacy studies
522 on A549^{+ACE2}. For viral growth kinetics, pooled media from P0 stock was used to plaque
523 purify a single virus clone on Vero E6 cells in presence of 1µg/ml TPCK-Trypsin, to avoid
524 virus adaptation to Vero E6 cells due to the lack of TMPRSS2 expression⁶⁶. Purified
525 plaques were sequenced to verify the signature clade B amino acid changes, S D614G
526 and NSP12 P323L, before expanding in presence of TPCK-Trypsin to generate a
527 passage 1 working stock (1.8 E + 06 PFU/mL).

528

529 **Characterization of A549^{+ACE2} cells.** Confluent 6-well A549 and A549^{+ACE2} cells were
530 washed with PBS and cells were detached with CellStripper dissociation reagent (Corning
531 cat no. 25056CI). Cells were pelleted, washed with PBS and either i) lysed in LDS sample
532 buffer (ThermoFisher cat no. NP0007) supplemented with reducing agent (ThermoFisher
533 cat no. NP0004) and Western blots were performed to analyze levels of ACE2 (1:1,000,
534 GeneTex cat no. GTX101395) with beta-actin (1:10,000, ThermoFisher cat no. MA5-
535 15739) as the loading control and imaged using Li-Cor Odyssey CLx, or ii) incubated in
536 FACS buffer (PBS, 5% FBS, 0.1% sodium azide, 1mM EDTA) for 30 min on ice followed
537 by 1 hour incubation with AlexaFluor 647 conjugated anti-ACE2 (1:40, R&D Biosystems

538 cat no.FABA9332R) or isotype control (1:40, R&D Biosystems cat no. IC003R) and
539 subsequent analysis on CytoFLEX flow cytometer. Surface ACE2 was visualized by
540 staining A549 and A549^{+ACE2} cells at 4°C with anti-ACE2 (1:500, R&D Biosystems AF933)
541 and AlexaFluor 647 secondary antibody and DAPI. Images were collected on the BZ-
542 X810 (RRID:SCR_016979, Keyence, Osaka, Japan) fluorescence microscope.

543 Confluent 6-well A549 and A549^{+ACE2} cells were collected in RLT lysis buffer
544 supplemented with beta-mercaptoethanol and total RNA was extracted using Qiagen
545 RNeasy mini kit. cDNA synthesis was performed using SuperScript™ III system
546 (ThermoFisher cat no. 18080051) followed by RT-qPCR with PowerUp SYBR Master Mix
547 (ThermoFisher cat no. A25742) on a QuantStudio 3 Real Time PCR System using gene-
548 specific primers pairs for ACE2 and RPS11 as the reference gene.
549 (ACE2fwd:GGGATCAGAGATCGGAAGAAGAAA,
550 ACE2rev:AGGAGGTCTAACATCATCAGTG,
551 RPS11fwd:GCCGAGACTATCTGCACTAC, RPS11rev:ATGTCCAGCCTCAGAACTTC).
552 A549 and A549^{+ACE2} cells were seeded in black wall 96-well plates and at confluence,
553 cells were infected with SARS-CoV-2. At 24 and 48 hpi, samples were fixed, stained with
554 mouse monoclonal SARS-CoV anti-N antibody 1C7, which cross reacts with SARS-CoV-
555 2 N (1:1000, kind gift of Thomas Moran), AlexaFluor 647 secondary antibody and DAPI,
556 and imaged using CellInsight CX7 LZR high-content screening platform. Images were
557 analyzed and quantified with HCS Navigator software. Syncytia were imaged using the
558 Keyence BZ-X810 microscope at 60X magnification on A549^{+ACE2} cultured on chambered

559 slides followed by 48 hpi SARS-CoV-2 infection and staining with SARS-CoV-2 N,
560 AlexaFluor 647 secondary antibody, and DAPI.

561
562 **SARS-CoV-2 growth kinetics on A549^{+ACE2} cells.** A549^{+ACE2} cells were seeded into 6-
563 cm dishes at 70% confluency. The next day, media was removed and cells were washed
564 twice with PBS with calcium and magnesium to remove residual medium. Cells were then
565 infected at 0.01 multiplicity of infection (MOI), based on A549^{+ACE2} titer, at 37°C. The
566 remaining inoculum was stored at -80°C for back titration. 1 hour post virus addition, virus
567 was removed, cells were washed twice with PBS with calcium and magnesium to remove
568 unbound virus and infection media (DMEM 2% FBS, 1% Pen/Strep, 1% NEAA, 10mM
569 HEPES) was added. 60 µl of supernatant were collected and stored at -80°C to determine
570 successful removal of input virus. Supernatant was then collected at 12, 24, 48 and 72
571 hpi, and stored at -80°C.

572 Viral titers in the supernatants were determined by focus forming assay. A549^{+ACE2} cells
573 were seeded into black wall 96-well plates at 70% confluency. The next day, cells were
574 then infected with 1:10 serial dilutions of the collected samples for 1 hour at 37°C. 1 hour
575 post virus addition, virus was removed, and cells were overlayed with MEM 1.8% Avicell,
576 1% Pen/Strep, 1% GlutaMax, 20mM HEPES, 0.4% BSA, 0.24% NaHCO₃. At 48 hours
577 post infection, the overlay was removed, and cells were fixed by submerging in 10%
578 formalin solution for 30-45 min. After fixation, cells were washed once with H₂O to remove
579 excess formalin. Plates were dried and PBS was added per well before exiting the BSL-
580 3 facility. Fixed cells were permeabilized with Triton-X and stained with mouse
581 monoclonal SARS-CoV anti-N antibody 1C7, which cross-reacts with SARS-CoV-2 N

582 (kind gift of Thomas Moran), goat anti-mouse AlexaFluor 647, and DAPI. Plates were
583 scanned on the CellInsight CX7 LZR high-content screening platform. A total of 9 images
584 were collected at 4X magnification to span the entire well. Infection foci were counted
585 manually.

586

587 **Human airway epithelial cultures (HAEC).** To generate HAEC, Bci-NS1.1 were plated
588 (7.5 E + 04 cells/well) on rat-tail collagen type 1-coated permeable transwell membrane
589 supports (6.5 mm; Corning, cat no. 3470), and immersed apically and basolaterally in
590 Pneumacult Ex Plus medium (StemCell, cat no. 05040). Upon reaching confluence,
591 medium was removed from the apical side (“airlift”), and medium in the basolateral
592 chamber was changed to Pneumacult ALI maintenance medium (StemCell, cat no.
593 05001). Medium in the basolateral chamber was exchanged with fresh Pneumacult ALI
594 maintenance medium every 2-3 days for 12-15 days to form differentiated, polarized
595 cultures that resemble *in vivo* pseudostratified mucociliary epithelium. Cultures were used
596 within 4-6 weeks of differentiation. HAEC were used for cytotoxicity assays and SARS-
597 CoV-2 infections.

598

599 **Compound acquisition, dilution, and preparation.** PF-00835231, remdesivir, and CP-
600 100356 were solubilized in 100% DMSO and provided by Pfizer, Inc. Compound stocks
601 diluted in DMSO to 30 mM were stored at -20°C. Compounds were diluted to 10 μ M
602 working concentration in complete media or Pneumacult ALI maintenance medium. All
603 subsequent compound dilutions were performed in according media containing DMSO
604 equivalent to 10 μ M compound. GC-376 was purchased from BPS Biosciences (cat no.

605 78013) and used at 10 μ M working concentration. SARS-CoV-2 (2019-nCov) rabbit
606 polyclonal spike neutralizing antibody from Sino Biological (cat no. 40592-R001) was
607 used at 3 μ M working concentration. As a positive control for cytotoxicity assays,
608 staurosporine was purchased from Sigma (cat no. S6942), and used at 1 μ M working
609 concentration.

610

611 **In vitro drug efficacy and cytotoxicity in A549^{+ACE2} cells.** A549^{+ACE2} cells were seeded
612 into black wall 96-well plates at 70% confluence. The next day, media was removed and
613 replaced with complete media containing compound/carrier two hours prior to infection.
614 Cells were then infected at 0.425 multiplicity of infection (MOI), based on Vero E6 titer, at
615 37°C. 1 hour post virus addition, virus was removed, and media containing
616 compound/carrier was added. At 24 and 48 hours post infection, cells were fixed by
617 submerging in 10% formalin solution for 30-45 min. After fixation, cells were washed once
618 with H₂O to remove excess formalin. Plates were dried and PBS was added per well
619 before exiting the BSL-3 facility. Fixed cells were permeabilized with Triton-X and stained
620 with mouse monoclonal SARS-CoV anti-N antibody 1C7, which cross-reacts with SARS-
621 CoV-2 N (kind gift of Thomas Moran), goat anti-mouse AlexaFluor 647, and DAPI. Plates
622 were scanned on the CellInsight CX7 LZR high-content screening platform. A total of 9
623 images were collected at 4X magnification to span the entire well. Images were analyzed
624 using HCS Navigator to obtain total number of cells/well (DAPI stained cells) and
625 percentage of SARS-CoV-2 infected cells (AlexaFluor 647 positive cells). To enable
626 accurate quantification, exposure times for each channel were adjusted to 25% of
627 saturation and cells at the edge of each image were excluded in the analysis. SARS-CoV-

628 2-infected cells were gated to include cells with an average fluorescence intensity greater
629 than 3 standard deviations that of mock infected and carrier treated cells. Representative
630 images of viral foci were acquired using the BZ-X810 at 40X magnification of plates fixed
631 at 48 hpi SARS-CoV-2 infection.

632 For determination of cytotoxicity, A549^{+ACE2} cells were seeded into opaque white wall 96-
633 well plates. The following day, media was removed, replaced with media containing
634 compound/carrier or staurosporine, and incubated for 24 or 48 hours, respectively. At
635 these timepoints, ATP levels were determined by CellTiter-Glo 2.0 (Promega, cat no.
636 G9242) using a BioTek Synergy HTX multi-mode reader.

637

638 **Time-of-drug-addition experiments.** A549^{+ACE2} cells seeded into black wall 96-well
639 plates and at confluence were treated and infected as followed. At 2.5 hours prior
640 infection, cells were pre-treated with complete media containing 1x compound/carrier. In
641 addition, SARS-CoV-2 (2x) was incubated with SARS-CoV-2 (2019-nCov) rabbit
642 polyclonal spike neutralizing antibody (nAB, 2x). Pre-treated cells and virus/neutralizing
643 antibody mix (1x) were incubated for 1 hour at 37°C. To synchronize infection, pre-
644 incubated plates and SARS-CoV-2/nAB mix were chilled at 4°C for 30 min and SARS-
645 CoV-2 was diluted on ice in media containing compound/carrier/nAB. Following pre-
646 chilling, virus/compound/carrier/nAB mixtures were added to the cells to allow binding of
647 virus for 1 hour at 4°C. Plates were moved to 37°C to induce virus entry and therefore
648 infection. 1 hour post virus addition, virus was removed, and complete media was added
649 to all wells. Complete media containing 2x compound/carrier/nAB was added to pre-
650 treated cells, cells treated at infection and cells treated at 1 hour post infection. At 2, 3

651 and 4 hours post infection, complete media containing compound/carrier/nAb was added
652 to according wells. At 12 hours post infection, samples were fixed, stained with SARS-
653 CoV-2 N, AlexaFluor 647 secondary antibody, and DAPI, and imaged using CellInsight
654 CX7 LZR high-content screening platform. Images were analyzed and quantified with
655 HCS Navigator software as described for in vitro efficacy in A549+ACE2.

656

657 **In vitro efficacy and cytotoxicity in human airway epithelial cultures (HAEC).** 48
658 hours prior to infection, 2-6-week-old HAEC were washed apically twice for 30 min each
659 with pre-warmed PBS containing calcium and magnesium, to remove mucus on the apical
660 surface. 2 hours prior to infection, HAEC were pretreated by exchanging the ALI
661 maintenance medium in the basal chamber with fresh medium containing compounds or
662 carrier. Remdesivir and PF-00835231 were used at 10, 0.5 and 0.025 μ M, and CP-
663 100356 at 1 μ M. 1 hour prior to infection, cultures were washed apically twice for 30 min
664 each with pre-warmed PBS containing calcium and magnesium. Each culture was
665 infected with 1.35E + 05 PFU (Vero E6) per culture for 2 hours at 37°C. A sample of the
666 inoculum was kept and stored at -80°C for back-titration by plaque assay on Vero E6
667 cells. For assessment of compound toxicity, additional cultures were washed and pre-
668 treated as the infected cultures. Instead of being infected, these cultures were incubated
669 with PBS containing calcium and magnesium only as Mock treatment. HAEC were
670 incubated with the viral dilution or Mock treatment for 2 hours at 37°C. The inoculum was
671 removed and the cultures were washed three times with pre-warmed PBS containing
672 calcium and magnesium. For each washing step, buffer was added to the apical surface
673 and cultures were incubated at 37°C for 30 min before the buffer was removed. The third

674 wash was collected and stored at -80°C for titration by plaque assay on Vero E6 cells.
675 Infected cultures were incubated for a total of 72 hours at 37°C. Infectious progeny virus
676 was collected every 12 hours by adding 60 µL of pre-warmed PBS containing calcium
677 and magnesium, incubation at 37°C for 30 min, and collection of the apical wash to store
678 at -80°C until titration. Additionally, trans-epithelial electrical resistance (TEER) was
679 measured in uninfected but treated HAEC to quantify the tissue integrity in response to
680 treatment with compounds or carrier. At the end point, cultures were fixed by submerging
681 in 10% formalin solution for 24 hours and washed three times with PBS containing calcium
682 and magnesium before further processing for histology. Alternatively, at the end point,
683 transwell membranes were excised and submerged in RLT buffer to extract RNA using
684 the RNAeasy kit (Qiagen, cat no. 74104). cDNA synthesis was performed using
685 SuperScript™ III system (ThermoFisher cat no. 18080051) followed by RT-qPCR with
686 TaqMan universal PCR master mix (ThermoFisher cat no. 4305719) and TaqMan gene
687 expression assay probes (ThermoFisher GAPDH cat no. 4333764F, BAX cat no.
688 Hs00180269_m1, BCL2 cat no. Hs00608023_m1) using a QuantStudio 3 Real Time PCR
689 System.

690 For additional determination of cytotoxicity in undifferentiated HAEC precursor cells, Bci-
691 NS1.1 cells were seeded into opaque white wall 96-well plates. The following day, media
692 was removed, replaced with media containing compound/carrier or staurosporine, and
693 incubated for 24 or 48 hours, respectively. At these timepoints, ATP levels were
694 determined by CellTiter-Glo 2.0 (Promega, cat no. G9242) using a BioTek Synergy HTX
695 multi-mode reader.

696

697 **Histology on human airway epithelial cultures.** For histology, transwell inserts were
698 prepared using a Leica Peloris II automated tissue processor, paraffin embedded, and
699 sectioned at 3 μ m. The resulting slides were stained using a modified Periodic Acid–Schiff
700 (PAS)-Alcian Blue protocol (Histotechnology, Freida L. Carson). Sections were imaged on
701 the Leica SCN whole slide scanner and files were uploaded to the Slidepath Digital Image
702 Hub database for viewing.

703

704 **Immunofluorescence on human airway epithelial cultures.** For immunofluorescence
705 of HAEC at top view, fixed and washed cultures were permeabilized with 50 mM NH₄Cl
706 (in PBS), 0.1% w/v saponin and 2% BSA (permeabilization/blocking (PB) buffer). Cultures
707 were stained with i) rabbit polyclonal anti-SARS Nucleocapsid Protein antibody, which
708 cross reacts with SARS-CoV-2 N (1:1000, Rockland cat no. 200-401-A50) and goat-anti-
709 rabbit AlexaFluor 488, to visualize infection ii) mouse monoclonal anti-ZO-1-1A12 (1:500,
710 Thermo Fisher cat no. 33-9100) and goat anti-mouse AlexaFluor 647 to visualize tight
711 junctions, and DAPI. All dilutions were prepared in PB buffer. Images were collected on
712 the Keyence BZ-X810 microscope.

713

714 **Single-cell RNA-seq analysis of human airway epithelial cultures.** 6-week-old human
715 airway cultures were used for the single-cell RNA-seq analysis. The apical surface was
716 washed once to remove mucus by adding 100 μ L of PBS and incubating for 30 min at
717 37°C. Cells were dissociated by cutting out the transwell membrane and incubating it in
718 700 μ L TrpLE 10x (Thermo Fisher cat no. A1217701) for 30 min rocking at 37°C. To
719 increase dissociation cells were pipetted through wide-bore tips every 10 min during the

720 incubation time. When cells were visually dissociated 700 μ l of ALI maintenance medium
721 supplemented with 0.1% Pluronic (Thermo Fisher cat. No. 24040032) was added and
722 cells were carefully pipetted again using wide-bore tips. The cell suspension was
723 centrifuged through a 10 μ M filter at 300 \times g for 5 min to break up any remaining cell
724 clumps. The cell pellet was washed once with 200 μ L ALI maintenance medium
725 supplemented with 0.1% Pluronic before cell number and viability was assed using the
726 Countess II (Thermo Fisher) to calculate cell numbers used in the following steps for
727 single-cell RNA-seq analysis.

728 Single-cell transcriptome profiling of dissociated organoids was carried out using the
729 Chromium Next GEM Single Cell 5' Library & Gel Bead Kit and Chromium controller (10X
730 genomics). To enable multiplexing and doublet detection, cells were stained with
731 barcoded antibodies described previously (Mimitou et al., 2019). Briefly, approximately
732 200,000 cells per sample were resuspended in staining buffer (PBS, 2% BSA, 0.01%
733 Tween) and incubated for 10 minutes with Fc block (TruStain FcX, Biolegend; FcR
734 blocking reagent, Miltenyi). Cells were then incubated with barcoded hashing antibodies
735 for 30 min at 4 °C. After staining, cells were washed 3 times in staining buffer. After the
736 final wash, cells were resuspended in PBS + 0.04% BSA, filtered, and counted. Cells
737 were pooled and loaded onto the Chromium chips. For each lane, we pooled 5 samples,
738 ~10,000 cells per sample. The single-cell capturing, barcoding, and cDNA library
739 preparation were performed using the Chromium Next GEM Single Cell 5' Library & Gel
740 Bead Kit by following the protocols recommended by the manufacturer. HTO additive
741 oligonucleotide was spiked into the cDNA amplification PCR and the HTO library was
742 prepared as described previously⁶⁷.

743 The Cellranger software suite (<https://support.10xgenomics.com/single-cell-gene-expression/software/pipelines/latest/what-is-cell-ranger>) from 10X was used to
744 demultiplex cellular barcodes, align reads to the human genome (GRCh38
745 ensemble, http://useast.ensembl.org/Homo_sapiens/Info/Index) and perform UMI
746 counting. From filtered counts HTODemux was used to demultiplex hash-tagged samples
747 and Seurat1 version 3.1.3 was used to process the single-cell data including dimension
748 reduction, UMAP representation and differential expression to identify cell type specific
749 markers determined by Wilcoxon test⁶⁸.
750

751

752 **In silico analysis of bronchoalveolar lavages (BAL).** Filtered gene-barcode matrices
753 for the BAL dataset were downloaded from GEO accession number GSE145926.
754 Matrices were normalized using ‘LogNormalize’ methods in Seurat v.3 with default
755 parameters and the resulting values were scaled using ScaleData. Seurat version 3.1.3
756 was used to process the single cell data including dimension reduction, UMAP
757 representation and differential expression to identify cell type specific markers determined
758 by Wilcoxon test.

759

760 **Statistical analysis.** Antiviral activities of PF-00835231 and remdesivir in A549^{+ACE2} cells
761 were determined by the following method. The percent inhibition at each concentration
762 was calculated by ActivityBase (IDBS) based on the values for the no virus control wells
763 and virus containing control wells on each assay plate. The concentration required for a
764 50% / 90% response (EC₅₀ / EC₉₀) was determined from these data using a 4-parameter
765 logistic model. Curves were fit to a Hill slope of 3 when >3 and the top dose achieved

766 $\geq 50\%$ effect. Geometric means and 95% confidence intervals were generated in
767 ActivityBase. Statistical comparisons were performed by log transforming the EC₅₀ and
768 EC₉₀ values and fitting separate linear models to each endpoint, assuming equal log-
769 scale variances across conditions and interactions of compound with strain and
770 compound with time. The model can be described mathematically as

771
$$\log EC_x = Treatment_i + \varepsilon_{i,j}, x = 50 \text{ or } 90$$

772 where $Treatment_i$ represents the effect of the combination of compound, strain, and time
773 and $\varepsilon_{i,j}$ represents a normal error term for treatment i and assay replicate j . Contrasts
774 between the factor combinations of interest were computed to assess significance and
775 back-transformed into ratios of geometric means. Statistical significance was defined by
776 a p value < 0.05 . Other statistical data analyses were performed in GraphPad Prism 7.
777 Statistical significance for each endpoint was determined with specific statistical tests as
778 indicated in each legend. For each test, a P-value < 0.05 was considered statistically
780 significant.

781 **References**

- 782 1. Zhu, N. *et al.* A novel coronavirus from patients with pneumonia in China, 2019. 783 *N. Engl. J. Med.* **382**, 727–733 (2020).
- 784 2. Gorbunova, A. E. *et al.* The species Severe acute respiratory syndrome-related 785 coronavirus: classifying 2019-nCoV and naming it SARS-CoV-2. *Nat. Microbiol.* **5**, 786 536–544 (2020).
- 787 3. Pruijssers, A. J. *et al.* Remdesivir Inhibits SARS-CoV-2 in Human Lung Cells and 788 Chimeric SARS-CoV Expressing the SARS-CoV-2 RNA Polymerase in Mice. *Cell 789 Rep.* **32**, 107940 (2020).
- 790 4. Ziebuhr, J. & Siddell, S. G. Processing of the Human Coronavirus 229E Replicase 791 Polyproteins by the Virus-Encoded 3C-Like Proteinase: Identification of 792 Proteolytic Products and Cleavage Sites Common to pp1a and pp1ab. *J. Virol.* 793 **73**, 177–185 (1999).
- 794 5. Gadlage, M. J. & Denison, M. R. Exchange of the Coronavirus Replicase 795 Polyprotein Cleavage Sites Alters Protease Specificity and Processing. *J. Virol.* 796 **84**, 6894–6898 (2010).
- 797 6. Dai, W. *et al.* Structure-based design of antiviral drug candidates targeting the 798 SARS-CoV-2 main protease. *Science (80-).* **335**, eabb4489 (2020).
- 799 7. Zhang, L. *et al.* Crystal structure of SARS-CoV-2 main protease provides a basis 800 for design of improved a-ketoamide inhibitors. *Science (80-).* **368**, 409–412 801 (2020).
- 802 8. Gordon, D. E. *et al.* A SARS-CoV-2 protein interaction map reveals targets for 803 drug repurposing. *Nature* **583**, 459–468 (2020).
- 804 9. Hoffman, R. L. *et al.* Discovery of Ketone-Based Covalent Inhibitors of 805 Coronavirus 3CL Proteases for the Potential Therapeutic Treatment of COVID-19. 806 *J. Med. Chem.* **63**, 12725–12747 (2020).
- 807 10. Yoshino, R., Yasuo, N. & Sekijima, M. Identification of key interactions between 808 SARS-CoV-2 main protease and inhibitor drug candidates. *Sci. Rep.* **10**, 12493 809 (2020).
- 810 11. Ma, C. *et al.* Boceprevir, GC-376, and calpain inhibitors II, XII inhibit SARS-CoV-2 811 viral replication by targeting the viral main protease. *Cell Res.* (2020). 812 doi:10.1038/s41422-020-0356-z
- 813 12. Jin, Z. *et al.* Structural basis for the inhibition of SARS-CoV-2 main protease by 814 antineoplastic drug carmofur. *Nat. Struct. Mol. Biol.* **27**, 529–532 (2020).
- 815 13. Jin, Z. *et al.* Structure of Mpro from SARS-CoV-2 and discovery of its inhibitors. 816 *Nature* (2020). doi:10.1038/s41586-020-2223-y
- 817 14. Boras, B. *et al.* Discovery of a Novel Inhibitor of Coronavirus 3CL Protease as a 818 Clinical Candidate for the Potential Treatment of COVID-19. *bioRxiv Prepr. Serv.* 819 *Biol.* (2020). doi:doi.org/10.1101/2020.09.12.293498
- 820 15. Bossennec, M., Di Roio, A., Caux, C. & Ménétrier-Caux, C. MDR1 in immunity: 821 friend or foe? *Oncoimmunology* **7**, 1–11 (2018).
- 822 16. Sankatsing, S. U. C., Beijnen, J. H., Schinkel, A. H., Lange, J. M. A. & Prins, J. M. 823 P Glycoprotein in Human Immunodeficiency Virus Type 1 Infection and Therapy. 824 *Antimicrobial Agents and Chemotherapy* (2004). doi:10.1128/AAC.48.4.1073- 825 1081.2004

826 17. Puelles, V. G. *et al.* Multiorgan and Renal Tropism of SARS-CoV-2. *N. Engl. J. Med.* **383**, 590–592 (2020).

827 18. Zou, L. *et al.* SARS-CoV-2 Viral Load in Upper Respiratory Specimens of Infected
828 Patients. *N. Engl. J. Med.* (2020). doi:10.1056/nejmc2001737

829 19. Daniel Blanco-Melo, Benjamin E. Nilsson-Payant, Wen-Chun Liu, Skyler Uhl, D.,
830 Hoagland, Rasmus Møller, Tristan X. Jordan, Kohei Oishi, Maryline Panis, D.,
831 Sachs, Taia T. Wang, Robert E. Schwartz, Jean K. Lim, Randy A. Albrecht1, B. &
832 TenOever, R. Imbalanced host response to SARS-CoV-2 drives development of
833 COVID-19. *Cell* (2020). doi:10.1016/j.cell.2020.04.026

834 20. Shannon, A. *et al.* Remdesivir and SARS-CoV-2: Structural requirements at both
835 nsp12 RdRp and nsp14 Exonuclease active-sites. *Antiviral Res.* **178**, 104793
836 (2020).

837 21. Rambaut, A. *et al.* A dynamic nomenclature proposal for SARS-CoV-2 lineages to
838 assist genomic epidemiology. *Nat. Microbiol.* (2020). doi:10.1038/s41564-020-
839 0770-5

840 22. Gonzalez-Reiche, A. S. *et al.* Introductions and early spread of SARS-CoV-2 in
841 the New York City area. *Science (80-)* **21**, eabc1917 (2020).

842 23. Plante, J. A. *et al.* Spike mutation D614G alters SARS-CoV-2 fitness. *Nature*
843 (2020). doi:10.1038/s41586-020-2895-3

844 24. Hou, Y. J. *et al.* SARS-CoV-2 D614G variant exhibits efficient replication ex vivo
845 and transmission in vivo. *Science (80-)* (2020). doi:10.1126/science.abe8499

846 25. Thornburg, N. *et al.* Data From ‘FDA Database for Regulatory Grade microbial
847 Sequences (FDA-ARGOS): Supporting development and validation of Infectious
848 Disease Dx tests’. GenBank Accession number MT233526.1 (2020).

849 26. Roder, A. *et al.* Data From: ‘SARS-CoV-2 sequences from COVID19 patients in
850 New York’. GenBank Accession number MT703677.1 (2020).

851 27. Lavi, E., Wang, Q., Weiss, S. R. & Gonatas, N. K. Syncytia formation induced by
852 coronavirus infection is associated with fragmentation and rearrangement of the
853 Golgi apparatus. *Virology* **221**, 325–334 (1996).

854 28. Corver, J., Broer, R., Van Kasteren, P. & Spaan, W. Mutagenesis of the
855 transmembrane domain of the SARS coronavirus spike glycoprotein: Refinement
856 of the requirements for SARS coronavirus cell entry. *Virol. J.* **6**, 1–13 (2009).

857 29. Kim, Y. *et al.* Broad-Spectrum Antivirals against 3C or 3C-Like Proteases of
858 Picornaviruses, Noroviruses, and Coronaviruses. *J. Virol.* **86**, 11754–11762
859 (2012).

860 30. Vuong, W. *et al.* Feline coronavirus drug inhibits the main protease of SARS-CoV-
861 2 and blocks virus replication. *Nat. Commun.* (2020). doi:10.1038/s41467-020-
862 18096-2

863 31. Gordon, C. J. *et al.* Remdesivir is a direct-acting antiviral that inhibits RNA-
864 dependent RNA polymerase from severe acute respiratory syndrome coronavirus
865 2 with high potency. *J. Biol. Chem.* **295**, 6785–6797 (2020).

866 32. Krichel, B., Falke, S., Hilgenfeld, R. & Redecke, L. Processing of the SARS-CoV
867 pp1a / ab nsp7 – 10 region. *0*, 1009–1019 (2020).

868 33. Agostini, M. L. *et al.* Coronavirus Susceptibility to the Antiviral Remdesivir (GS-
869 5734) Is Mediated by the Viral Polymerase and the Proofreading
870 Exoribonuclease. *MBio* **9**, (2018).

871

872 34. Daelemans, D., Pauwels, R., De Clercq, E. & Pannecouque, C. A time-of-drug
873 addition approach to target identification of antiviral compounds. *Nat. Protoc.* **6**,
874 925–933 (2011).

875 35. Reid, A. T. *et al.* Ground zero-the airway epithelium. in *Rhinovirus Infections: Rethinking the Impact on Human Health and Disease* (2019). doi:10.1016/B978-0-12-816417-4.00003-2

876 36. Garcíá, S. R. *et al.* Novel dynamics of human mucociliary differentiation revealed
877 by single-cell RNA sequencing of nasal epithelial cultures. *Development (Cambridge)* **146**, (2019).

878 37. Ravindra, N. *et al.* Single-cell longitudinal analysis of SARS-CoV-2 infection in
879 human airway epithelium. *bioRxiv Prepr. Serv. Biol.* (2020).
880 doi:10.1101/2020.05.06.081695

881 38. Dittmann, M., Koralov, S. B. & Ruggles, K. Data From: 'Analysis of 3D human
882 airway epithelial cultures by single-cell RNA-seq'. GEO series GSE166601
883 (2020).

884 39. Greaney, A. M. *et al.* Platform Effects on Regeneration by Pulmonary Basal Cells
885 as Evaluated by Single-Cell RNA Sequencing. *Cell Rep.* **30**, 4250–4265.e6
886 (2020).

887 40. Suzuyama, N. *et al.* Species differences of inhibitory effects on P-glycoprotein-
888 mediated drug transport. *J. Pharm. Sci.* (2007). doi:10.1002/jps.20787

889 41. Walters, M. S. *et al.* Generation of a human airway epithelium derived basal cell
890 line with multipotent differentiation capacity. *Respir Res* **14**, 135 (2013).

891 42. Liao, M. *et al.* Single-cell landscape of bronchoalveolar immune cells in patients
892 with COVID-19. *Nat. Med.* **26**, 842–844 (2020).

893 43. Liao, M. *et al.* Data From 'Single-cell landscape of bronchoalveolar immune cells
894 in COVID-19 patients'. GEO series GSE145926 (2020).

895 44. Hui, K. P. Y. *et al.* Tropism, replication competence, and innate immune
896 responses of the coronavirus SARS-CoV-2 in human respiratory tract and
897 conjunctiva: an analysis in ex-vivo and in-vitro cultures. *Lancet Respir. Med.*
898 **2600**, 1–9 (2020).

899 45. Chu, H. *et al.* Comparative tropism, replication kinetics, and cell damage profiling
900 of SARS-CoV-2 and SARS-CoV with implications for clinical manifestations,
901 transmissibility, and laboratory studies of COVID-19: an observational study. *The Lancet Microbe* (2020). doi:10.1016/s2666-5247(20)30004-5

902 46. Sheahan, T. P. *et al.* An orally bioavailable broad-spectrum antiviral inhibits
903 SARS-CoV-2 in human airway epithelial cell cultures and multiple coronaviruses
904 in mice. *Sci. Transl. Med.* **12**, (2020).

905 47. Cao, B. *et al.* A trial of lopinavir-ritonavir in adults hospitalized with severe covid-
906 19. *N. Engl. J. Med.* (2020). doi:10.1056/NEJMoa2001282

907 48. Ma, C. *et al.* Boceprevir, GC-376, and calpain inhibitors II, XII inhibit SARS-CoV-2
908 viral replication by targeting the viral main protease. *Cell Res.* (2020).
909 doi:10.1038/s41422-020-0356-z

910 49. Deng, X. *et al.* Coronaviruses Resistant to a 3C-Like Protease Inhibitor Are
911 Attenuated for Replication and Pathogenesis, Revealing a Low Genetic Barrier
912 but High Fitness Cost of Resistance. *J. Virol.* (2014). doi:10.1128/jvi.01528-14

913 50. Günthard, H. F. *et al.* Human Immunodeficiency Virus Drug Resistance: 2018

918 Recommendations of the International Antiviral Society-USA Panel. *Clin. Infect. Dis.* (2019). doi:10.1093/cid/ciy463

919

920 51. Su, T. H. & Liu, C. J. Combination therapy for chronic hepatitis B: Current updates and perspectives. *Gut and Liver* (2017). doi:10.5009/gnl16215

921

922 52. Whitley, R. J. & Monto, A. S. Resistance of Influenza Virus to Antiviral Medications. *Clin. Infect. Dis.* (2019). doi:10.1093/cid/ciz911

923

924 53. Kumar, A. Early versus late oseltamivir treatment in severely ill patients with 2009 pandemic influenza A (H1N1): Speed is life. *J. Antimicrob. Chemother.* (2011). doi:10.1093/jac/dkr090

925

926

927 54. Wölfel, R. *et al.* Virological assessment of hospitalized patients with COVID-2019. *Nature* (2020). doi:10.1038/s41586-020-2196-x

928

929 55. Jonathan Grein, M. D. *et al.* Compassionate Use of Remdesivir for Patients with Severe Covid-19. *N. Engl. J. Med.* (2020).

930

931 56. Chaudhary, P. M., Mechetner, E. B. & Roninson, I. B. Expression and activity of the multidrug resistance P-glycoprotein in human peripheral blood lymphocytes. *Blood* (1992). doi:10.1182/blood.v80.11.2735.2735

932

933

934 57. Egashira, M., Kawamata, N., Sugimoto, K., Kaneko, T. & Oshimi, K. P-glycoprotein expression on normal and abnormally expanded natural killer cells and inhibition of P-glycoprotein function by cyclosporin A and its analogue, PSC833. *Blood* (1999). doi:10.1182/blood.v93.2.599.402k06_599_606

935

936

937

938 58. Chen, M. L. *et al.* Physiological expression and function of the MDR1 transporter in cytotoxic T lymphocytes. *J. Exp. Med.* (2020). doi:10.1084/jem.20191388

939

940 59. Cao, W. *et al.* The Xenobiotic Transporter Mdr1 Enforces T Cell Homeostasis in the Presence of Intestinal Bile Acids. *Immunity* (2017). doi:10.1016/j.jimmuni.2017.11.012

941

942

943 60. Fung, K. L. *et al.* MDR1 synonymous polymorphisms alter transporter specificity and protein stability in a stable epithelial monolayer. *Cancer Res.* (2014). doi:10.1158/0008-5472.CAN-13-2064

944

945

946 61. Gralinski, L. E. & Menachery, V. D. Return of the coronavirus: 2019-nCoV. *Viruses* **12**, 1–8 (2020).

947

948 62. Volz, E. *et al.* Transmission of SARS-CoV-2 Lineage B.1.1.7 in England: Insights from linking epidemiological and genetic data. *medRxiv* (2021).

949

950 63. Tegally, H. *et al.* Major new lineages of SARS-CoV-2 emerge and spread in South Africa during lockdown. *medRxiv* (2020). doi:10.1101/2020.10.28.20221143

951

952 64. Faria, N. & Et-al. *Genomic characterisation of an emergent SARS-CoV-2 lineage in Manaus: preliminary findings - SARS-CoV-2 coronavirus / nCoV-2019 Genomic Epidemiology - Virological.* virological.org (2021).

953

954

955 65. Seifert, L. L. *et al.* The ETS transcription factor ELF1 regulates a broadly antiviral program distinct from the type I interferon response. *PLoS Pathog.* (2019). doi:10.1371/journal.ppat.1007634

956

957

958 66. Johnson, B. A. *et al.* Loss of furin cleavage site attenuates SARS-CoV-2 pathogenesis. *Nature* 1–10 (2021). doi:10.1038/s41586-021-03237-4

959

960 67. Stoeckius, M. *et al.* Cell Hashing with barcoded antibodies enables multiplexing and doublet detection for single cell genomics. *Genome Biol.* (2018). doi:10.1186/s13059-018-1603-1

961

962

963 68. Stuart, T. *et al.* Comprehensive Integration of Single-Cell Data. *Cell* (2019).

964 doi:10.1016/j.cell.2019.05.031
965
966

967 **Figure legends**

968

969 **Figure 1. Validation of A549^{+ACE2} cells as a tool to study SARS-CoV-2.** A549^{+ACE2}
970 cells were generated by lentiviral transduction delivering an ACE2 overexpression
971 construct and subsequent bulk-selection. **a.-e.** ACE2 expression in A549 parental or
972 A549^{+ACE2} cells determined by RT-qPCR (**a.**), western blot (**b.**, quantified in **c.**), flow
973 cytometry (**d.**), or microscopy (**e.**). **f.** A549 parental or A549^{+ACE2} cells were infected with
974 a serial dilution of SARS-CoV-2 USA-WA1/2020. At 24 h, cells were fixed, stained for
975 SARS-CoV-2 N protein, and infected cells were quantified by high-content microscopy.
976 Means \pm SEM from duplicate wells. **g.** A549^{+ACE2} cells were infected with SARS-CoV-2
977 USA-WA1/2020 or USA/NYU-VC-003/2020 at MOI 0.01, and infectious progeny titers,
978 collected from supernatants over time, determined by focus forming assay on A549^{+ACE2}
979 cells. Means \pm SEM from n=3 independent experiments. Unpaired t-test, *p<0.05,
980 ***p<0.001, ****p<0.0001. **h.** Confocal microscopy of SARS-CoV-2 syncytia in A549^{+ACE2}
981 cells at 48 hpi.

982

983 **Figure 2. Antiviral SARS-CoV-2 activity and cytotoxicity of PF-00835231, and**
984 **remdesivir in A549^{+ACE2} cells.** **a.** Antiviral assay workflow. A549^{+ACE2} cells were
985 pretreated with serial dilutions of PF-00835231 or remdesivir, then infected with SARS-
986 CoV-2 while continuing drug treatment. At 24 or 48 h, cells were fixed, stained for SARS-
987 CoV-2 N protein, and infected cells quantified by high-content microscopy. Cytotoxicity
988 was measured in similarly treated but uninfected cultures via CellTiter-Glo assay. EC₅₀,
989 EC₉₀ and CC₅₀ from n=3 independent experiments are listed in Table 1. **b.** PF-00835231,

990 and **c.** remdesivir antiviral activity and cytotoxicity in A549^{+ACE2} cells infected with SARS-
991 CoV-2 USA-WA1/2020 for 24 h. Representative graphs shown. **d.** PF-00835231, and **e.**
992 remdesivir antiviral activity and cytotoxicity in A549^{+ACE2} cells infected with SARS-CoV-2
993 USA/NYU-VC-003/2020 for 24 h. Representative graphs shown. **f.** Representative
994 images of SARS-CoV-2 USA-WA1/2020 syncytia formation at 48 hpi in A549^{+ACE2} cells
995 under treatment with 0.33 μ M PF-00835231, or remdesivir.

996

997 **Figure 3. Antiviral SARS-CoV-2 activity and cytotoxicity of PF-00835231, and GC-**
998 **376 in A549^{+ACE2} cells.** Antiviral assay workflow as described in Fig. 2a. **a.** PF-00835231,
999 and **b.** GC-376 antiviral activity and cytotoxicity in A549^{+ACE2} cells infected with SARS-
1000 CoV-2 USA-WA1/2020 for 24 h. Representative graphs shown. **c.** PF-00835231, and **d.**
1001 GC-376 antiviral activity and cytotoxicity in A549^{+ACE2} cells infected with SARS-CoV-2
1002 USA/NYU-VC-003/2020 for 24 h. Representative graphs shown. **e.** Representative
1003 images of SARS-CoV-2 USA-WA1/2020 syncytia formation at 48 hpi in A549^{+ACE2} cells
1004 under treatment with 1 μ M PF-00835231, or GC-376.

1005

1006 **Figure 4. Time-of-drug-addition assay for PF-00835231, GC-376, remdesivir, and a**
1007 **neutralizing antibody in A549^{+ACE2} cells.** **a.** At the indicated time points, A549^{+ACE2} cells
1008 were infected with SARS-CoV-2 USA-WA1/2020, treated with 3 μ M monoclonal
1009 neutralizing antibody (control targeting attachment and entry), 10 μ M of the drug GC-376
1010 (control drug for 3CL^{pro} inhibition), 3 μ M PF-00835231 (3CL^{pro} inhibitor), or 10 μ M
1011 remdesivir (RdRp inhibitor). At 12 h (one round of replication) cells were fixed, stained for
1012 SARS-CoV-2 N protein, and infected cells quantified by high-content microscopy. Means

1013 \pm SEM from n=3 independent experiments. **b.** Schematic of SARS-CoV-2 life cycle in
1014 A549^{+ACE2} cells. 3CL^{pro}, 3C-like protease; RdRp, RNA-dependent RNA polymerase.

1015

1016 **Figure 5. Cell composition of polarized human airway epithelial cultures (HAEC),**
1017 **and cytotoxicity of PF-00835231 and remdesivir. a.** Schematic representation of a
1018 transwell containing a polarized HAEC in air-liquid interface. Dark blue, cycling basal
1019 cells; light blue, basal cells; red, suprabasal cells; purple, secretory cells; yellow, microfold
1020 cells; green, ciliated cells; grey, mucus. To test for cytotoxicity, drugs were added to the
1021 media in the basolateral chamber. **b.** Clustered UMAP of single cells determined by
1022 single-cell RNA sequencing from n=3 uninfected HAEC. Clusters were determined by
1023 markers from the literature^{36,37} and by differentially expressed marker genes for each
1024 cluster determined by Wilcox test. **c., d.** Representative cross-sections of uninfected
1025 HAEC, 72 h post treatment with 10 μ M PF-00835231 or 10 μ M remdesivir. H&E (**c.**) or
1026 PAS-Alcian blue staining (**d.**). **e.** Trans-epithelial resistance (TEER) in drug-treated,
1027 uninfected HAEC over time as a measure of epithelial integrity. Means \pm SEM from n=3
1028 independent experiments. **f.** CellTiter-glo assay on undifferentiated, basal-like Bci-NS1.1
1029 precursor cells. Means \pm SEM from n=3 independent experiments.

1030

1031 **Figure 6. Comparative anti-SARS-CoV-2 activity of PF-00835231 and remdesivir in**
1032 **polarized human airway epithelial cultures (HAEC).** To test for antiviral activity, drugs
1033 were added to the basolateral chamber, cultures infected with SARS-CoV-2 from the
1034 apical side, and apical washes collected in 12 h increments to determine viral titers by
1035 plaque assay. **a, b.** SARS-CoV-2 USA-WA1/2020 infectious titers from HAEC treated with

1036 incremental doses of remdesivir (**a.**) or PF-00835231 (**b.**). **c.** Representative top views of
1037 HAEC at 72 hpi; drug doses 0.3 μ M. Blue, DAPI (nuclei); cyan, ZO-1 (tight junctions); red,
1038 SARS-CoV-2 N protein (infected).

1039

1040 **Figure 7. Role of MDR1 drug efflux transporter for PF-00835231-mediated SARS-**
1041 **CoV-2 inhibition in human airway cells. a.** Schematic of experimental setup for (**b.-d.**).
1042 MDR1, encoded by ORF *ABCB1*, exports PF-00835231 from cells. CP-100356 was used
1043 as a chemical inhibitor to block MDR1 function. **b, c.** PF-00835231 antiviral activity and
1044 cytotoxicity in A549^{+ACE2} cells infected with SARS-CoV-2 USA-WA1/2020 for 24 (**b.**), or
1045 48 hpi (**c.**) in the presence or absence of 1 μ M MDR1 inhibitor CP-100356. Means \pm SEM
1046 from n=3 independent experiments. **d.** Apical SARS-CoV-2 USA-WA1/2020 infectious
1047 titers from HAEC treated basolaterally with 0, 0.025, or 0.5 μ M PF-00835231 in the
1048 presence or absence of 1 μ M MDR1 inhibitor CP-100356. Means \pm SEM from n=3
1049 independent experiments. **e.** Clustered UMAP of single cells from bronchoalveolar
1050 lavages of n=12 patients. Integrated data of healthy patients (n=3) and COVID-19 patients
1051 with mild (n=3) or severe (n=6) symptoms. **f.** Normalized expression of *ABCB1* in
1052 clustered single cells from (**e.**). Left y-axis depicts level of ABCB1 expression; right y-axis
1053 depicts % of ABCB1-positive cells, also indicated by black bars; % of cells within each
1054 population with detectable ABCB1 transcripts shown above for each population.

1055 **Data availability**

1056 All scRNA-seq data in this study can be accessed in GEO under the accession numbers
1057 GSE166601 and GSE145926.

1058

1059 **Acknowledgements**

1060 We would like to thank Thomas M Moran, Icahn School of Medicine at Mount Sinai, and
1061 Luis Martínez-Sobrido, Texas Biomedical Institute, for the kind gift of mouse monoclonal
1062 SARS-CoV N antibody 1C7. Histopathology of human airway cultures was performed by
1063 Mark Alu, Branka Brukner Dabovic and Cynthia Loomis from the NYUMC Experimental
1064 Pathology Research Laboratory. We are also grateful for to Adriana Heguy from the NYU
1065 Genome Technology Core. Both the Experimental Pathology Research Laboratory and
1066 the NYU Genome Technology Core are supported by NYU Cancer Center Support Grant
1067 P30CA016087, and NYU Langone's Laura and Isaac Perlmutter Cancer Center.
1068 Statistical analysis of antiviral activities in A549^{+ACE2} cells was performed by Woodrow
1069 Burchett. We thank Ralf Duerr for critical reading of the manuscript. Research was further
1070 supported by grants from NIH/NIAID (R01AI143639 and R21AI139374 to MD,
1071 T32AI17647 to RAP, R01HL125816 to SBK), by Jan Vilcek/David Goldfarb Fellowship
1072 Endowment Funds to AMVJ, by The G. Harold and Leila Y. Mathers Charitable
1073 Foundation to MD, by a NYU PI Pilot Grant to SBK, by Pfizer Inc. to MD, and by NYU
1074 Grossman School of Medicine Startup funds to MD.

1075

1076 **Author contributions**

1077 MdV, ASM, JB, ASA, and MD conceived and designed the study. MdV, ASM, AMVJ,
1078 RAP, AS, PL, EI performed the experiments and analyzed the data. CS, RO, JB analyzed
1079 antiviral data. MdV, ASM, AMVJ, RAP, KR, SBK, LD, JB, MD interpreted the data. MdV,
1080 ASM, LD, SBK and MD wrote the paper.

1081

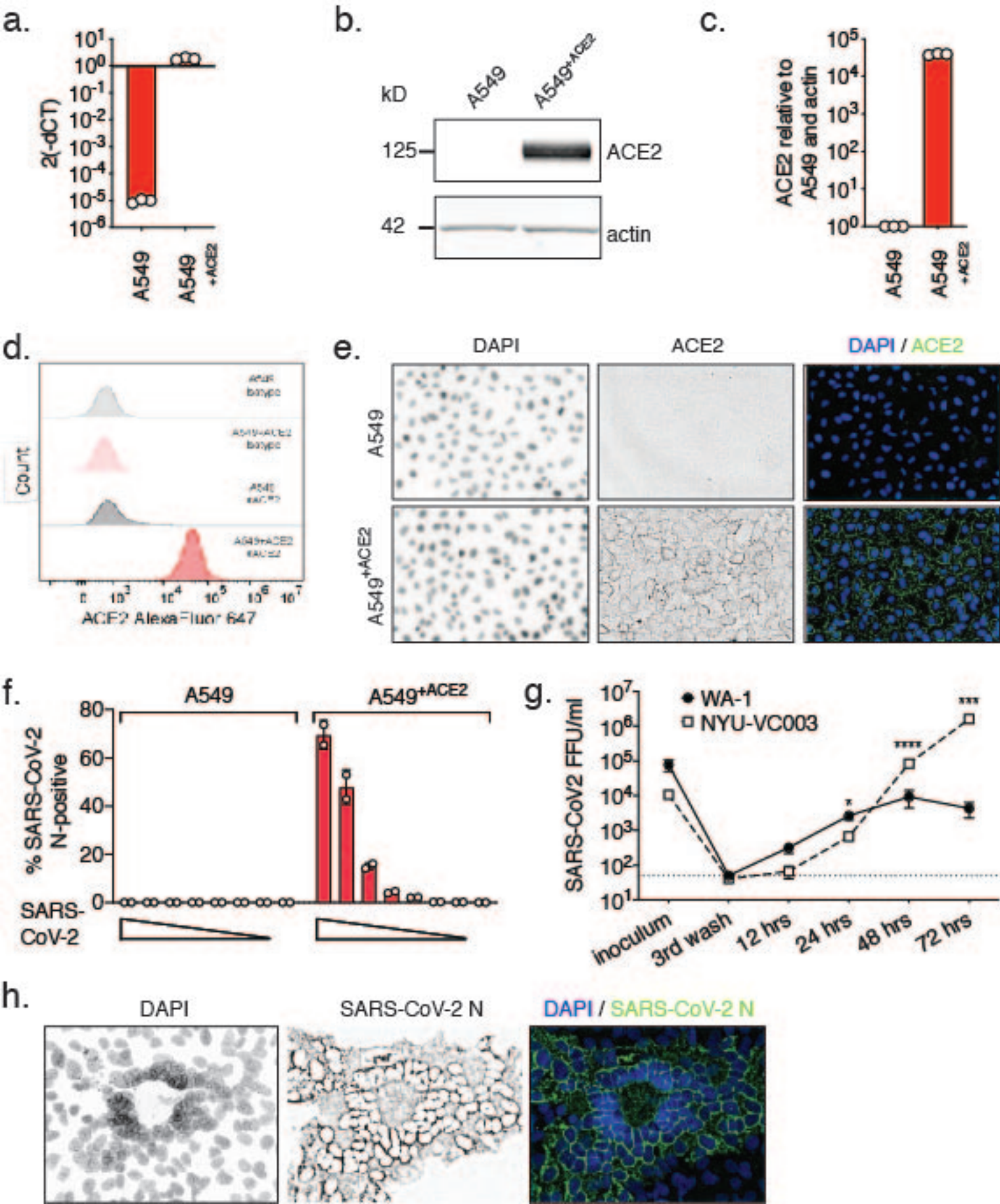
1082 **Competing interests**

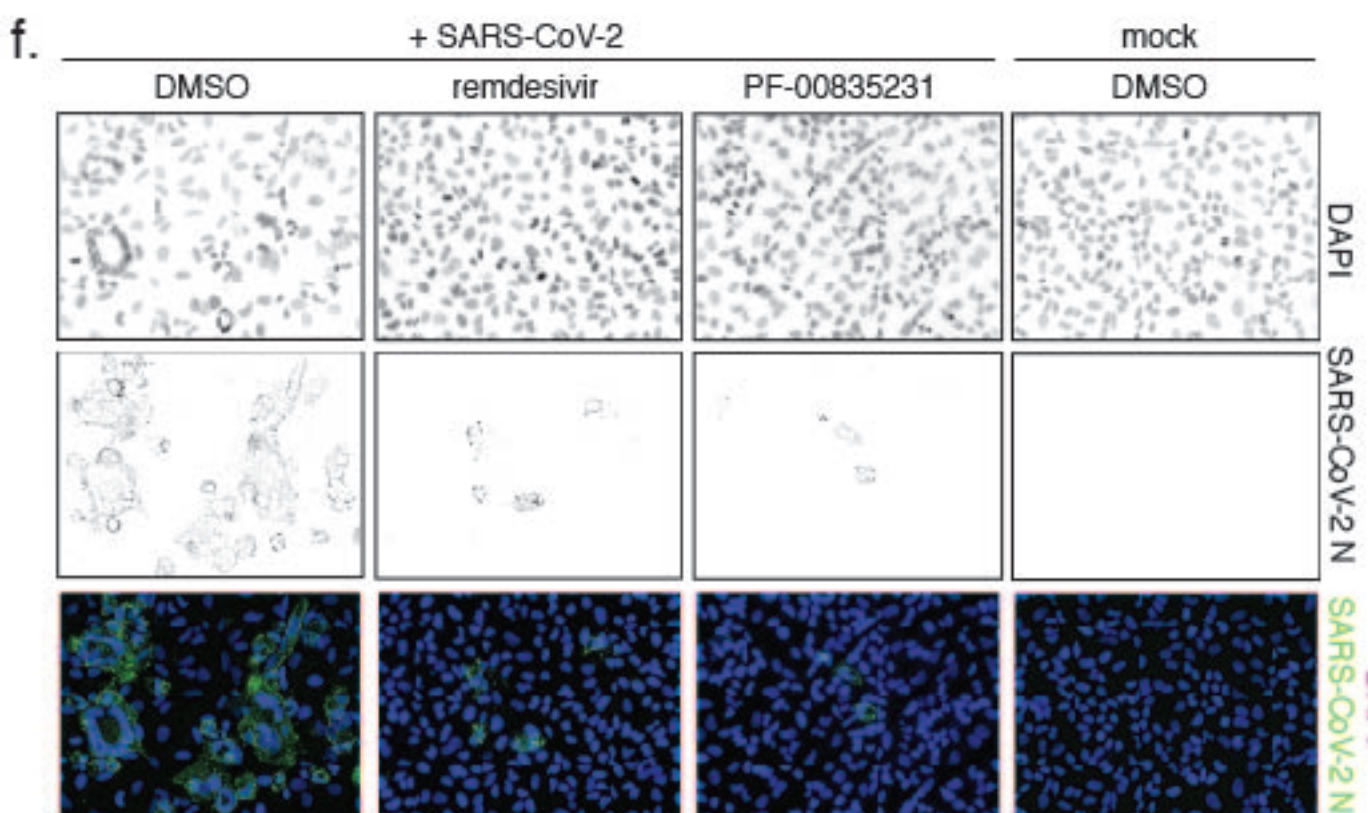
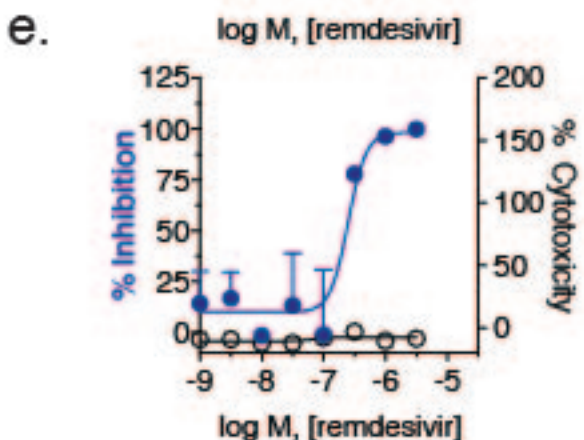
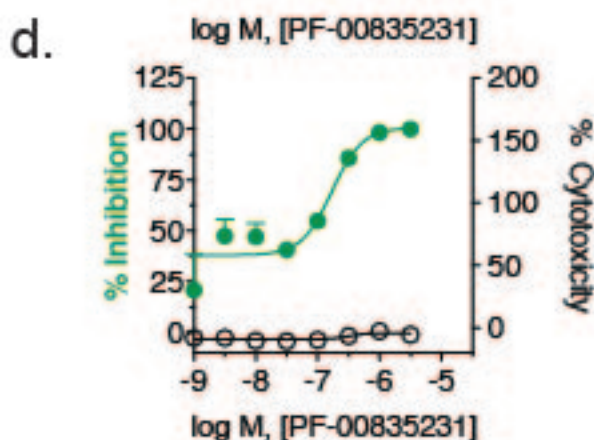
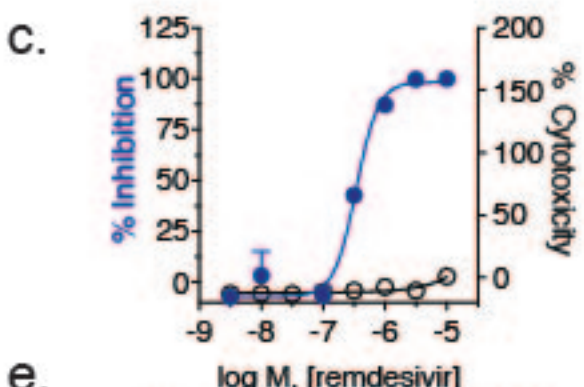
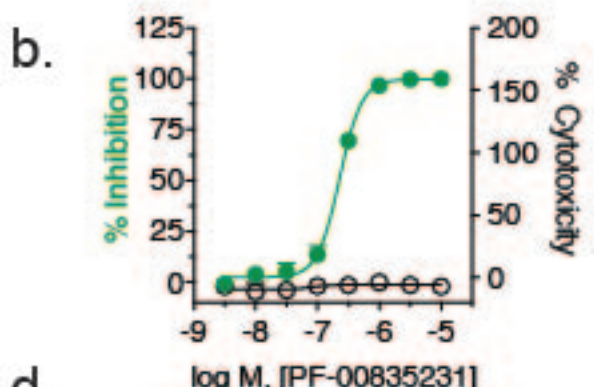
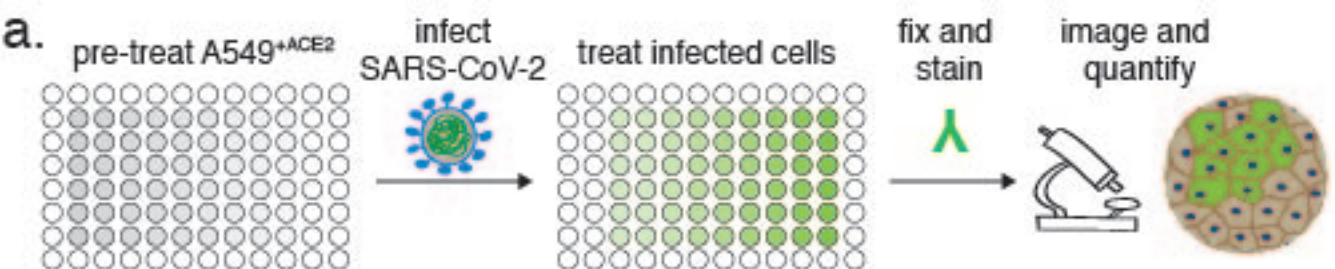
1083 M. D. received a contract from Pfizer Inc. to support the studies reported herein. These
1084 authors are employees of Pfizer Inc. and hold stock in Pfizer Inc: Joseph Binder,
1085 Annaliesa Anderson, Claire Steppan, Rebecca O'Connor.

1086

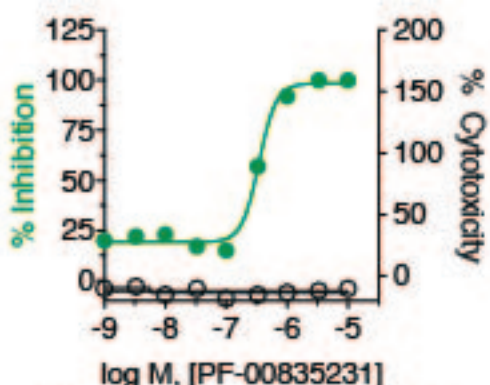
1087 **Materials and correspondence**

1088 All correspondence and material requests except those for antiviral compounds should
1089 be addressed to Meike.Dittmann@nyulangone.org. Compound requests should be
1090 addressed to Annaliesa.Anderson@pfizer.com.

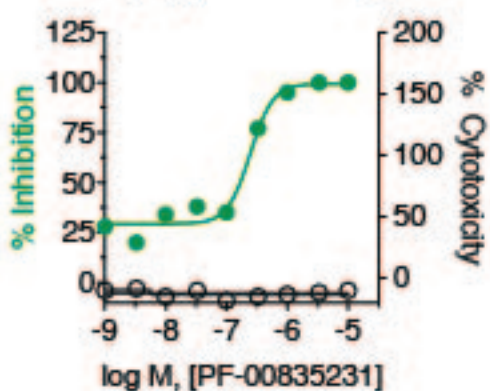




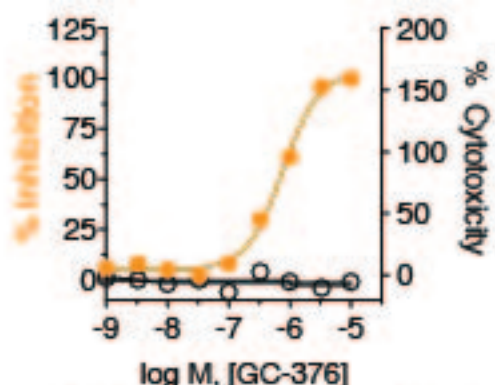
a.



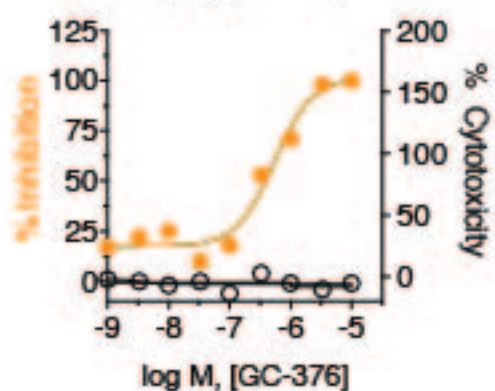
c.



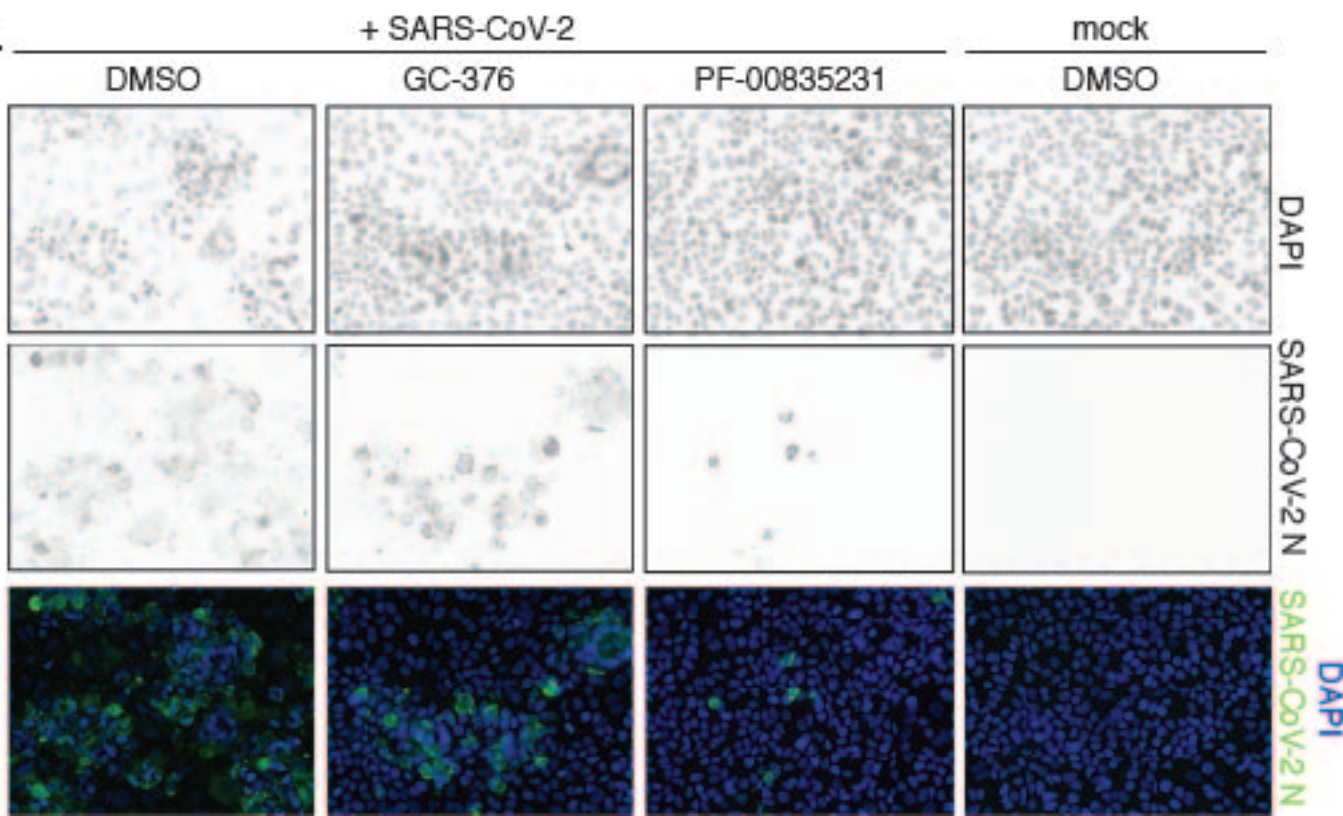
b.

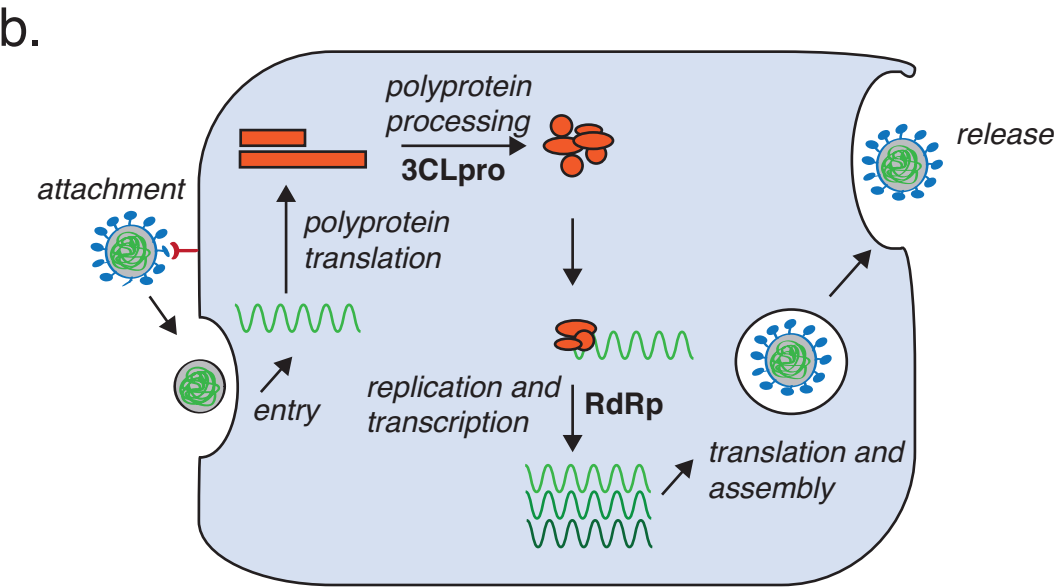
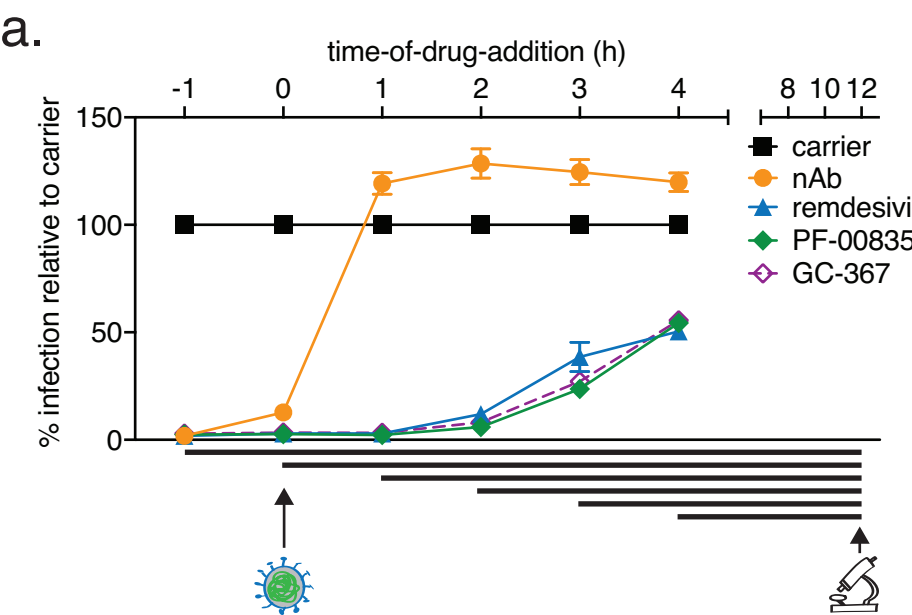


d.

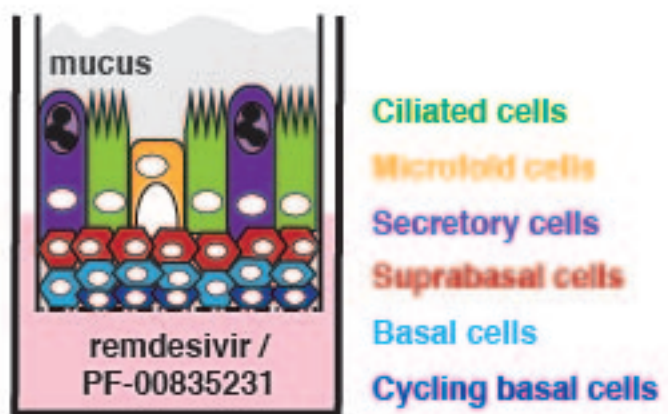


e.

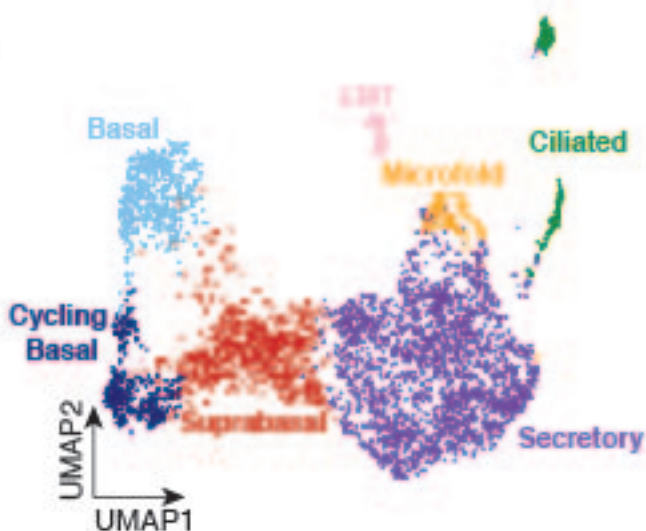




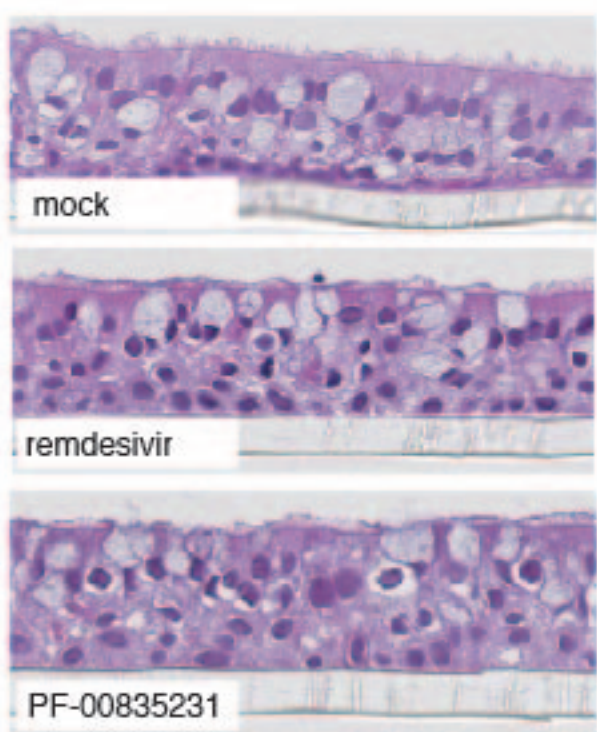
a.



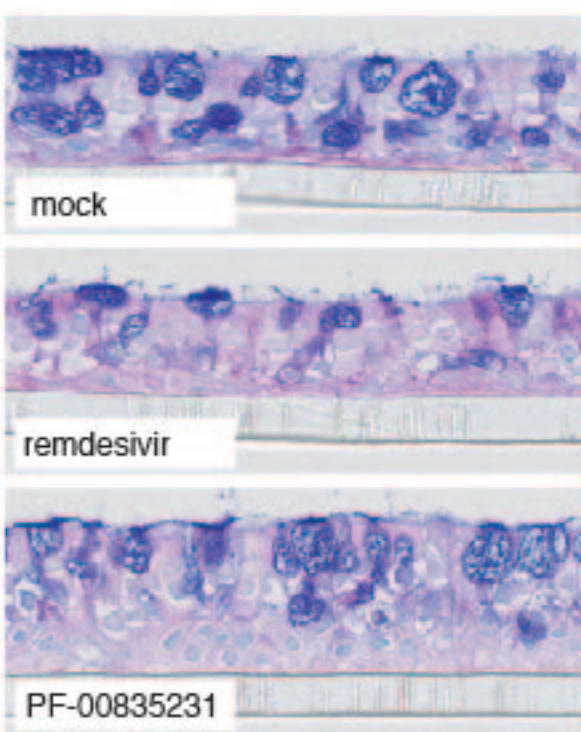
b.



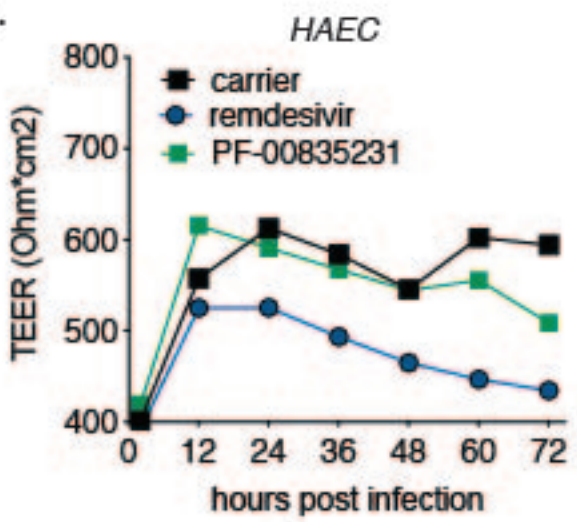
c.



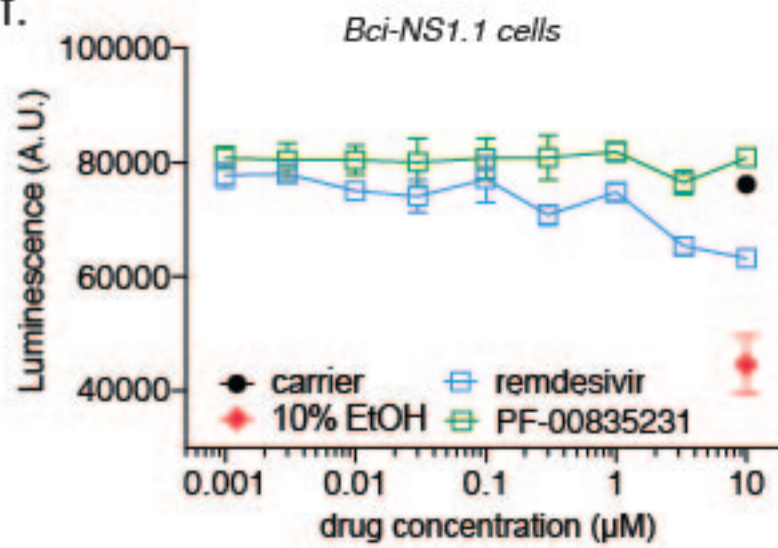
d.

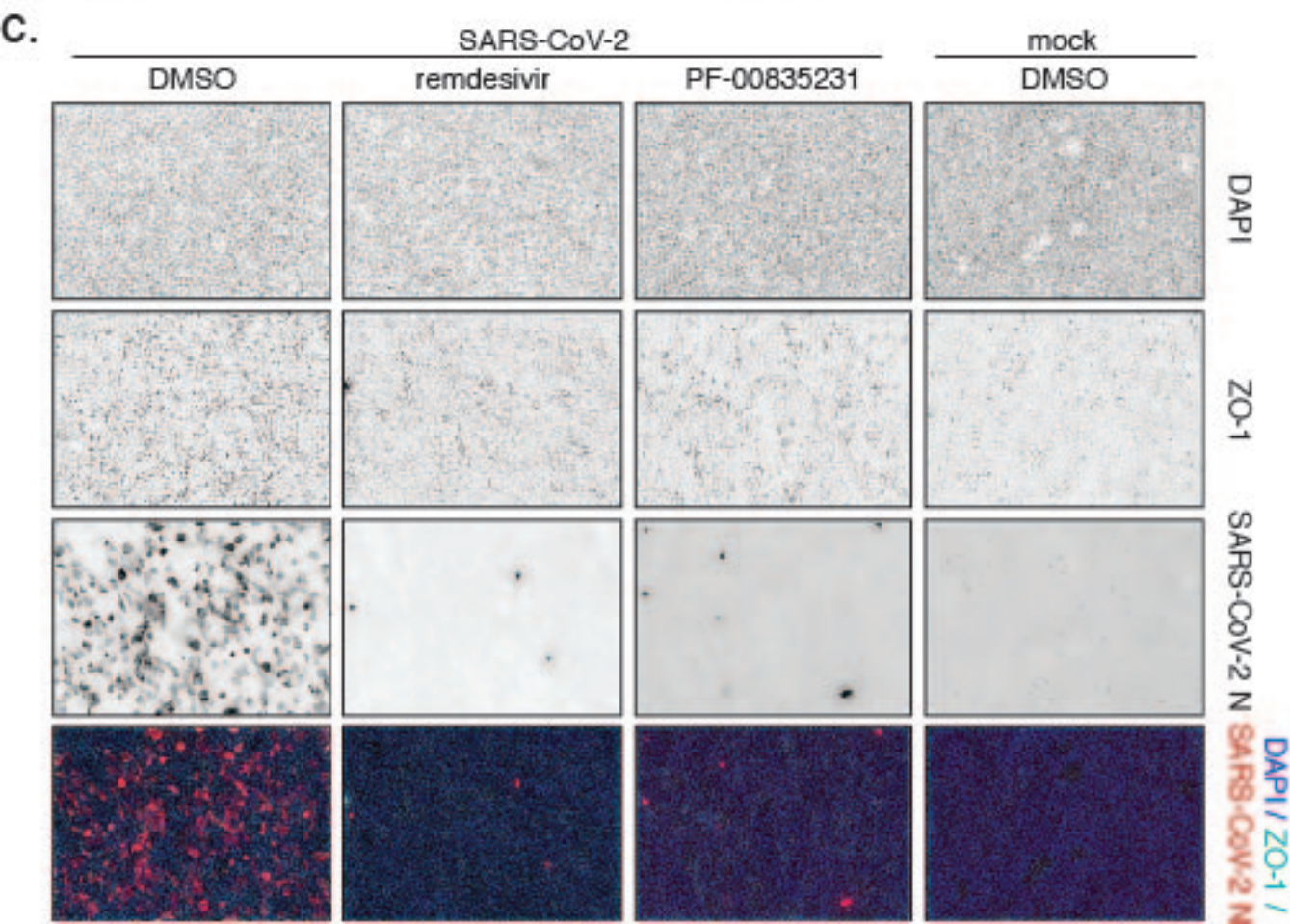
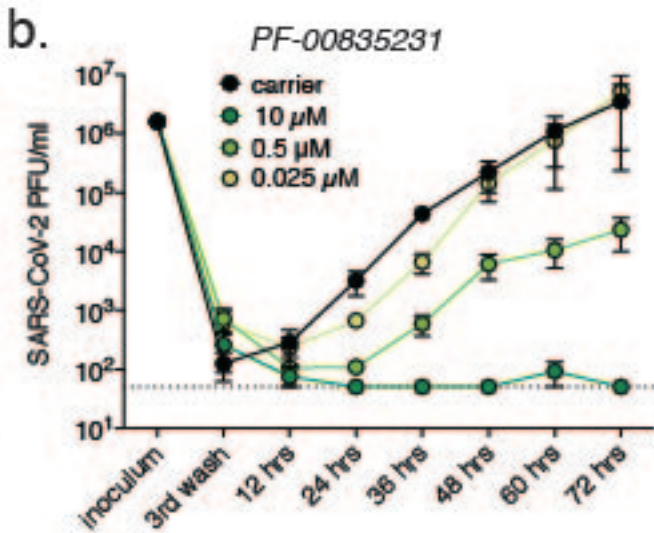
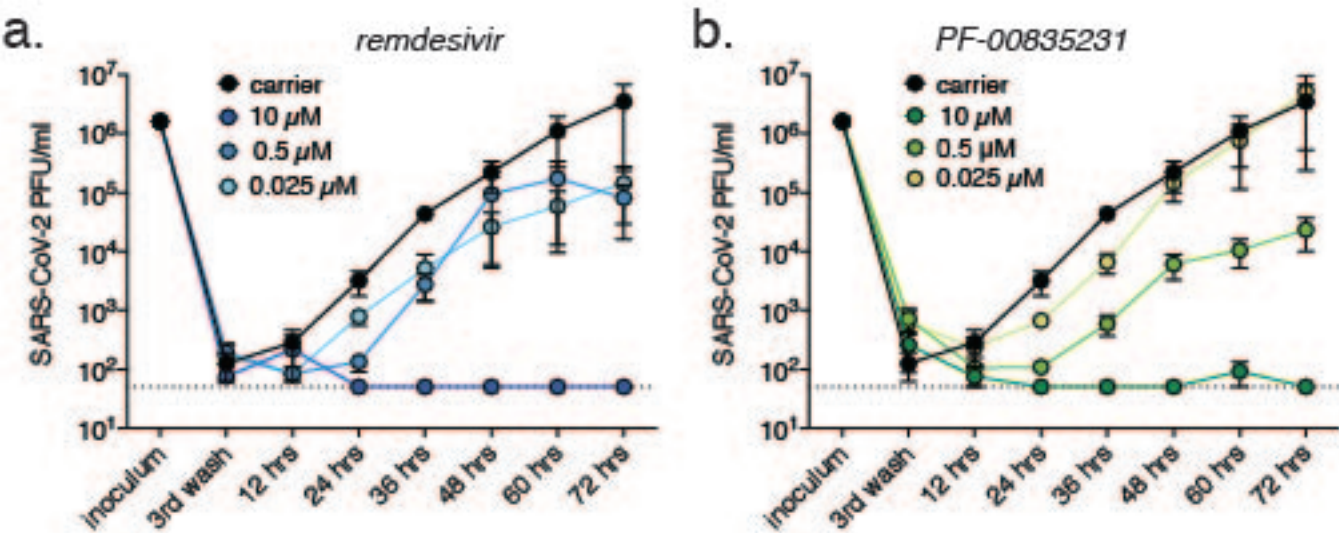


e.

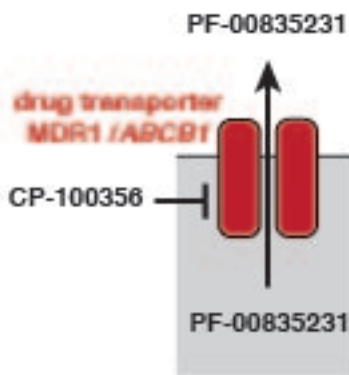


f.

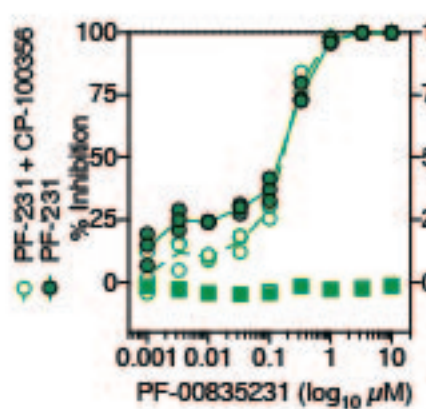




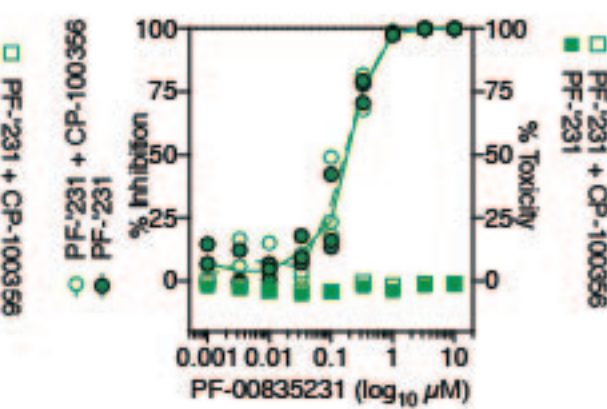
a.



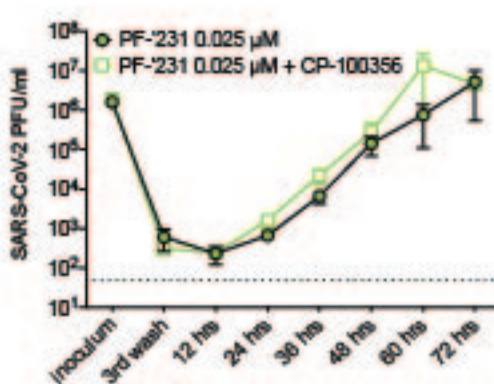
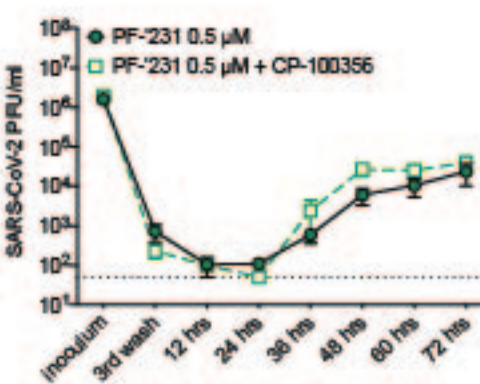
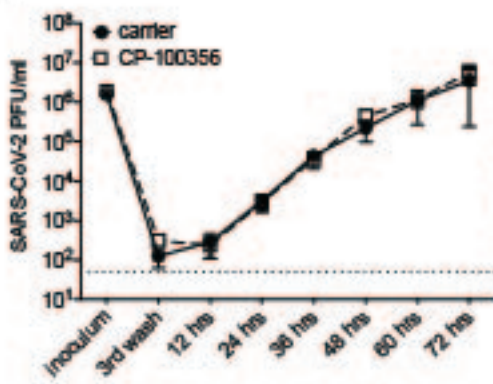
b.



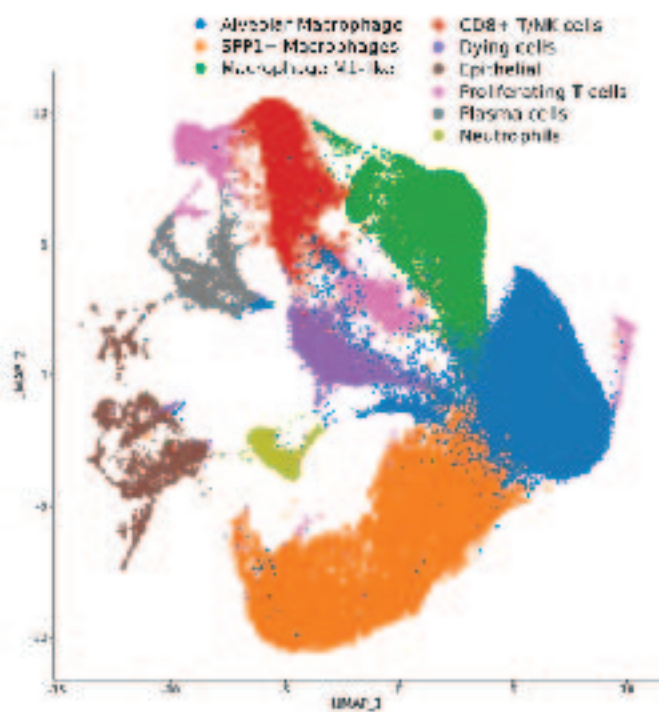
c.



d.



e.



f.

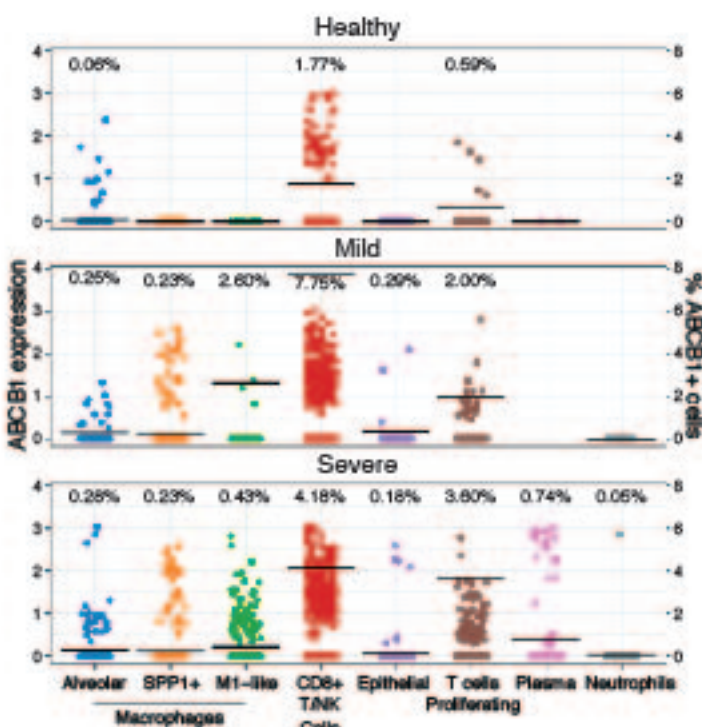


Table 1. Antiviral efficacy and cytotoxicity of PF-00835231 versus remdesivir on A549+ACE2 cells

USA-WA1/2020							
time	EC50 μ M	(95% CI)	p value*	p value**	EC90 μ M	(95% CI)	CC50 μ M
PF-00835231	24 hpi	0.221	0.137 -0.356		0.734	0.391-1.38	> 10
	48 hpi	0.158	0.0795 - 0.314		0.439	0.380-0.508	> 10
remdesivir	24 hpi	0.442	0.240-0.814	0.002	1.19	0.622-2.28	> 10
	48 hpi	0.238	0.122-0.436	0.035	0.529	0.534-0.656	> 10
USA/NYU-VC-003/2020							
time	EC50 μ M	(95% CI)	p value*	p value**	EC90 μ M	(95% CI)	CC50 μ M
PF-00835231	24 hpi	0.184	0.016-0.377		0.307	0.591	0.534-0.654
	remdesivir	24 hpi	0.238	0.200-0.400	0.028	0.024	0.589

* EC50 of remdesivir vs EC50 of PF-00835231

** EC50 of drug vs EC50 of same drug for USA-WA1/2020

Table 2. Antiviral efficacy and cytotoxicity of PF-00835231 versus GC-376 on A549+ACE2 cells

USA-WA1/2020							
time	EC50 μ M	(95% CI)	p value*	p value**	EC90 μ M	(95% CI)	CC50 μ M
PF-00835231	24 hpi	0.422	0.0836 - 2.13		0.978	0.326 - 2.93	>10
	48 hpi	0.344	0.0842 - 1.404		1.158	0.358 - 3.74	>10
GC-376	24 hpi	0.623	0.257 - 1.506	0.366	4.55	1.89 - 10.91	>10
	48 hpi	0.696	0.198 - 2.44	0.114	5.25	2.53 - 10.875	>10
USA/NYU-VC-003/2020							
time	EC50 μ M	(95% CI)	p value*	p value**	EC90 μ M	(95% CI)	CC50 μ M
PF-00835231	24 hpi	0.326	0.098 - 1.08		0.543	1.17	0.115 - 11.89
	24 hpi	0.529	0.184 - 1.512	0.265	0.700	2.734	0.897 - 8.33

* EC50 of GC-376 vs EC50 of PF-00835231

** EC50 of drug vs EC50 of same drug for USA-WA1/2020